

Title

Subtitle

by

Mikkel Metzsch Jensen

THESIS

for the degree of

MASTER OF SCIENCE



Faculty of Mathematics and Natural Sciences  
University of Oslo

Spring 2023



Title

Subtitle

Mikkel Metzsch Jensen



© 2023 Mikkel Metzsch Jensen

Title

<http://www.duo.uio.no/>

Printed: Reprosentralen, University of Oslo



# Abstract

Abstract.



# Acknowledgments

Acknowledgments.



# Contents

<b>List of symbols?</b>	<b>vii</b>
<b>Introduction</b>	<b>1</b>
0.1 Motivation	1
0.1.1 Friction	1
0.1.2 Thesis	1
0.2 Approach	1
0.3 Objective of the study	2
0.4 Contributions	2
0.5 Thesis structure	2
<b>1 Background Theory and Method</b>	<b>3</b>
1.1 Tribology - friction	3
1.1.1 Macroscale	3
1.1.1.1 Amontons' law	3
1.1.2 Microscopic scale	4
1.1.2.1 Surface roughness - Asperity theories	4
1.1.3 Nanoscale - Atomic scale	5
1.1.3.1 Frenkel-Kontorova	6
1.1.3.2 Experimental procedures	10
1.1.3.3 (summary of) Expected frictional properties	11
1.2 Molecular Dynamics	12
1.2.1 Potentials	12
1.2.1.1 General formulation of potentials (?)	13
1.2.1.2 Lennard Jones	13
1.2.1.3 Stillinger weber	13
1.2.1.4 Tersoff	14
1.2.2 Integration	16
1.2.2.1 Velocity Verlet	16
1.2.3 Thermostats	17
1.2.3.1 Langevin thermostat	17
1.2.3.2 Implementing Langevin	19
1.2.4 MD limitations (?)	20
1.2.5 LAMMPS	20
1.3 Defining the system	20
1.3.1 Region definitions (Sheet, pullblocks and substrate)	20
1.3.2 Numerical procedure	22
1.3.3 Creating the sheet	22
1.3.3.1 Graphene	22
1.3.3.2 Indexing	23
1.3.3.3 Removing atoms	24
1.3.4 Kirigami patterns	25
1.3.4.1 Pop-up	25
1.3.4.2 Honeycomb	25

1.3.4.3 Random walk	25
1.4 Pressure reference	25
1.5 Fourier Transform (light)	25
1.6 Machine Learning (ML)	26
1.6.1 Feed forward network / Neural networks	26
1.6.2 CNN for image recognition	26
1.6.3 GAN (encoder + deoder)	26
1.6.4 Inverse desing using machine learning	26
1.6.5 Prediction explanation	26
1.6.5.1 Shapley	26
1.6.5.2 Lineariations	26
1.6.5.3 LRP	26
1.6.5.4 t-SNE	26
<b>Simulations</b>	<b>27</b>
1.7 Baseline study	27
1.7.1 Variable overview	27
1.7.2 Raw data analysis	29
1.7.2.1 Force oscillations	29
1.7.2.2 Decompositions	30
1.7.2.3 Center of mass path	31
1.7.3 Defining metrics for dynamic and static friction	32
1.7.3.1 Dynamic friction	32
1.7.3.2 Static friction	33
1.7.4 Investigating selected parmeters	36
1.7.5 Normal force and stretch dependencies	38
1.7.5.1 Multi stretch	38
1.7.5.2 Multi normal force	39
1.7.5.3 Contact area	40
1.7.6 Computational cost	40
1.8 Generating data	41
1.9 Training forward network	41
1.10 Inverse design	41
1.11 Negative friction coefficient	41
1.11.1 Simulated coupling of normal force and stretch	41
1.11.2 Nanomachine coupling	41
<b>Summary</b>	<b>43</b>
1.12 Summary and conclusion	43
1.13 Outlook / Perspective	43

# List of symbols?

Maybe add list of symbols and where they are used like Trømborg.



# Introduction

## 0.1 Motivation

### 0.1.1 Friction

Friction is a fundamental force that takes part in almost all interactions with physical matter. Even though the everyday person might not be familiar with the term “friction” we would undoubtedly notice its disappearing. Without friction, it would not be possible to walk across a flat surface, lean against the wall or secure an object by the use of nails or screws (Static friction allows us to join objects together using screws [1][p. 5]). Similarly, we expect a moving object to eventually come to a stop if not supplied with new energy, and we know intuitively that sliding down a snow covered hill is much more exciting than its grassy counterpart. It is probably safe to say that the concept of friction is well integrated in our everyday life to such an extent that most people take it for granted. However, the efforts to control friction dates back to the early civilization (3500 B.C.) with the use of the wheel and lubricants to reduce friction in translational motion [2]. Friction is a part of the wider field tribology derived from the Greek word *Tribos* meaning rubbing and includes the science of friction, wear and lubrication [2].

The most important motivation to study tribology is ultimately to gain full control of frictional and wear for various technical applications. Especially, reducing friction is of great interest as this has tremendous advantages regarding energy efficiency. It has been reported that that monetary value of tribological problems has significant potential for economic and environmental improvements [3]:

“On global scale, these savings would amount to 1.4% of the GDP annually and 8.7% of the total energy consumption in the long term.” [4].

The reduction of friction is not the only sensible application as a controlled increase in friction might be of interest in the development of grasping robots or perhaps breaking system (get some sourced examples maybe...).

To the best of my knowledge kirigami has not yet been implemented to alter the friction properties in a similar manner as done in this thesis.

### 0.1.2 Thesis

In this thesis we investigate the possibility to control the frictional properties of a graphene sheet by applying strategically positioned cuts to the sheet inspired by kirigami. Kirigami is a variation of origami where the paper is cut additionally to being folded. Hanakata et al. [5] has shown that kirigami inspired cuts on a graphene sheet can be used to alter the yield strain and yield stress of the sheet. They observed that the stretching of the cutted sheet induced a out-of-plane buckling which serves as a key observation for the motivation of this thesis. It is currently well established/believed that the friction between two surfaces is proportional to the real microscopic contact area (source here?). Hence, one can hypothesize that the buckling of the sheet will affect the contact area and consequently the frictional properties.

## 0.2 Approach

In the study by Hanakata et al. [5] they used a machine learning (ML) approach to overcome the complexity of the nonlinear effects arrising from the out-of-plane buckling which made them successfully map the cutting patterns to the mechanical properties of yield and stress. The dataset used for the ML training was generated by molecular dynamics (MD) simulations for a limited set of cut configuration. By training the network the

MD simulaitions could effectively be skipped all together making for an accelerated search through new cut configurations for certain mechanical properties. By setting up a MD simulation that qunatifies the frictional properties of the graphene sheet we aim to make an analog study regarding the search for certain frictional properties.

We will take this on step further by creating a GAN network that utilises the latter network for creating an inverse design framework. That is, a network that takes frictional properties as input and return the corresponding cut configuration. By having such a tool we can execute a targeted search for exotic frictional properties. Particularly, we are interested in nonlinear and possibly even negative friction coefficients. Friction is essentially observed to increase with increasing load on the frictional surface, and we often describe this as having a positive friction coefficient. However, if we are able to couple the stretching of the sheet with friction we might be able to break this barrier for the coefficient. By imagining some nanomachine which translates downward pressure into either compression or expansion of the altered graphene, we could have a coupling between downward pressure and stretch of the sheet. In that case, a friction force depending on stretch could effectively be made to decrease with increasing load which would correspond to a negative friciton coefficient following this definition (formulate such that we do not imply free acceleration from nothing).

One of the features from inverse design, seperating it from the general class of ML approaches, is that we do not depend on trusting the ML predictions. While a standard neural network might be extremely efficient on a certain prediciton task we have usually no information on how these predictions are based. We say that the internal workings of the network is a black box beyond our capaacity of interpretation. However, for the inverse design problem we are prompted with a few promising design proposals which can immediately be tested in the MD simulations which we will regard as the most reliable predictor in this setting. Hence, if arriving at a successful design in alignment our search prompt, we can disregard any uncertainty in the network. In that case the remaining gap to bridge is that of the MD simulation and real life implementations.

### 0.3 Objective of the study

1. Design a MD simulation to evaluate the frictional properties of the grpahene sheet under different variations of cut patterns, stretching and loading, among other physical variables.
2. Train a network to replace the MD simulation completely.
3. (Variation 1) Do an accelerated search using the ML network for exotic frictional properties such as low and friction coefficients and a strong coupling between stretch and friction.
4. (Variation 2) Make a GAN network using the first network and predict cut configurations for some of the above mentiond frictional properties.
5. (If I have time) Make a nanomachine that couples load and stretch (perhaps just artificially without any molecular mechanism) to test the hypothesize of a negativ friction coefficient.

### 0.4 Contributions

What did I actually achieve

### 0.5 Thesis structure

How is the thesis structured.

# Chapter 1

# Background Theory and Method

Small introtext to motivate this chapter. What am I going to go over here.

## 1.1 Tribology - friction

Friction is a part of the wider field tribology which includes the study of friction, wear and lubrication between two surfaces in relative motion [1, p. 1]. In this thesis we will only concern ourselves with so-called wearless dry friction. That is, without any use of lubrication and without any resulting wear of the contacting surfaces. Tribological systems take place across a broad range of time and length scales, ranging from geological stratum layers involved in earthquakes [3] to microscopic atomistic processes, as in the gliding motion of a nanocluster of a nanomotor [6]. This vast difference in scale gives rises to different frictional mechanism being dominating at different scales. On a macro scale the system is usually subject to relatively high loads and speeds leading to high contact stresses and wear. On the other hand, the micro-/nanoscale regime occupies the opposite domain operating under relatively small loads and speeds with negligible wear [3] [2, p. 5]. While macroscale friction is often reduced into a few variables such as load, material type, speed and surface roughness it is clear that the micro-/nanoscale friction cannot be generalized under such a simple representation. On the micro-/nanoscale the tribological properties dominated by surface properties which will introduce an additional sensitivity variables such as temperature, humidity and even sliding history. The works of Bhushan and Kulkarni [7, (1996)] showed that the friction coefficient decreased with scale even though the materials used was unchanged. This reveals an intrinsic relationship between friction and scale as the contact condition is altered.

The phenomenological descriptions of macroscale friction cannot yet be derived from the fundamental atomic principles, and bridging the gap between different length scales in tribological systems remains an open challenge [6]. Hence, the following sections will be organized into macro-, micro- and nanoscale representing the theoretical understanding governing each scale regime. While our study of the graphene sheet is based on a nanoscale perspective the hypothesizing about application possibilities will eventually draw upon a macroscale perspective as well. Thus, we argue that a brief theoretical introduction to all three major scales is of high interest for a more complete interpretation of the findings in this thesis.

### 1.1.1 Macroscale

Our working definition of the *macroscale* is everything on the scale of visible everyday objects, which is usually denoted to the size of millimeters  $10^{-3}$  m and above. Most importantly, we want to make a distinction to the *microscale*, where the prefix indicates the size of micrometers  $m^{-6}$ , and hence we essentially assign everything larger than *micro* to the term *macroscale*<sup>1</sup>.

#### 1.1.1.1 Amontons' law

In order to start and keep a solid block moving against a solid surface we must overcome certain frictional forces  $F_{\text{fric}}$  [1]. The static friction force  $F_s$  corresponds to the minimum tangential force required to initiate the sliding

<sup>1</sup>The width of a human hair is on the length scale  $10^{-5}$  to  $10^{-4}$  m which constitute a reasonable boundary between macro- and microscale which fit well with a lower bound of human perception capabilities.

while the kintec friciton force  $F_k$  corresponds to the tangential force needed to sustain such a sliding at steady speed. The work of Leonardo da Vinci (1452–1519), Guillaume Amontons (1663–705) and Charles de Coulomb (1736–1806) all contributed to the empirical law, commonly known as Amontons' law, which is a common friction model for the macroscale regime. Amontons' law states that the fricitonal forces is entirely independent of contact area and sliding velocity (at ordinary sliding velocities). Instead, it relies only on the normal force<sup>2</sup>  $F_N$ , acting perpendicular to the surface, and the material specific friction coefficient  $\mu$  as

$$F_{\text{fric}} = \mu F_N. \quad (1.1)$$

The friction coefficient is typically different for the cases of static ( $\mu_s$ ) and kinetic ( $\mu_k$ ) friction, usually with values lower than one and  $\mu_s \geq \mu_k$  in all cases [1, p. 6].

Allthough Amontons' law has been succesfull in the modelling of macroscale friction it has its limitations. For instance, it was later discovered that the static friction is not independent of time. It depends on the so-called contact history with increasing friction as the logarithm of time of stationary contact [8]. For the kinetic friction the independency of sliding velocity disappears at low velocities as thermal effects becomes important and for high velocities due to inertial effetc. [1, pp. 5-6].

Additionally, due to the emperical foundation, Amontons' law does not provide a physical insight into the underlying mechanisms of friction. However, as we will later discuss in more detail, we can understand the overall phenomena of friction through statistical mechanics by the concept of *equipartition of energy* [6]. A system in equilibrium has its kinetic energy uniformly distributed among all its degrees of freedom. When a macroscale object is sliding in a given direction it is clearly not in equilibrium since one of its degrees of freedom carries considerable more kinetic energy. Thus, the system will have a tendency to transfer that kinetic energy to the remaining degrees of freedom as heat. This heat will dissipate to the sourroundings and the object will slow down as a result. Hence, friction is really just the tendency of going toward equilibrium energy equipartitioning among many interacting degrees of freedom [6]. From this point of view it is clear that friction is an inevitable part of contact physics, but even though friction can be removed altogether, we are still capable of manipulating it in usefull ways.

The attentive reader might point out that we have already moved the discussion partly into the microscopic regime as *statistical mechanics* generally aim to explain macroscale behaviour by microscopic interactions. In fact this highlight the nessecity to consider smaller scales in order to achieve a more in depth understadning of friction.

### 1.1.2 Microscopic scale

Going from a macro- to microscale perspective, a length scale of order  $10^{-6}$  m, it was realized that most surfaces is in fact rough [9]. The contact between two surfaces consist of numerous smaller contact point, so-called asperities, for which the friction between two opposing surfaces involves interlocking of those asperities as visualized in figure 1.1. It is generally accepted that friction is caused by two mechanism: mechanical friction and chemical friction [3]. The mechanical friction is the “plowing” of the surface by hard particles or said asperities with an energy loss associated attributed deformations of the asperity. While plastic deformations, corresponding to wear, is obviously expected to act as an energy sink, elastic deformations is also sufficient in explaining energy loss due to phonon excitations. The chemical friction arrises from adhesion between microscopic contacting surfaces, with an energy loss assigned to breaking and forming of bonds.

#### 1.1.2.1 Surface roughness - Asperity theories

Asperity theories are based on the observation that microscopic rough surfaces, with contacting asperities each with a contact area of  $A_{\text{asp}}$ , will have a true contact area  $\sum A_{\text{asp}}$  much smaller than the apperent macrosopic area  $A_{\text{macro}}$  [3]. The friction force was shown to be proportional to the true contact area as

$$F_{\text{fric}} = \tau \sum A_{\text{asp}},$$

where  $\tau$  is an effective shear strength of the contacting bodies. Note that this is still compatible with Amontons' law in eq. (1.1) if we find a linear relatiohsip between the real contact area and the applied normal force  $F_N$ . In

---

<sup>2</sup>Normal force is often used interchangeably with the terms *load* and *normal load*.

figure 1.1 we see a visualization on how the contact area might intuitively increase with normal force as the asperity tips is deformed into broader contact points.

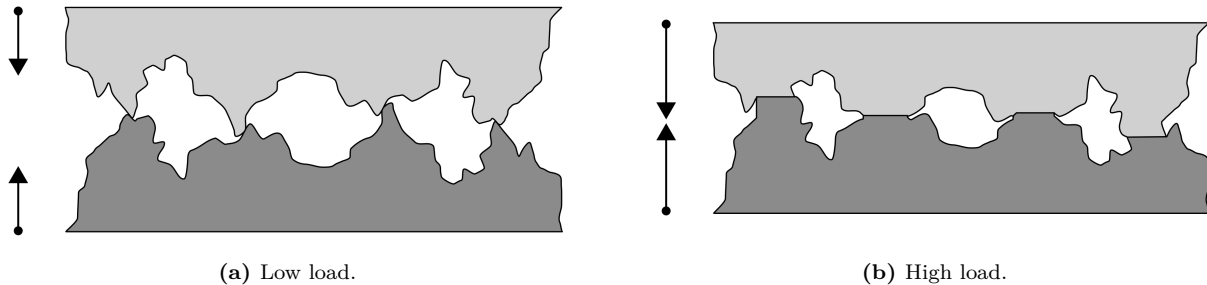


**Figure 1.1:** Qualitatively illustration of the microscopic asperity deformation under increasing load from frame a to b [10].

Many studies have focused on single asperity contacts to reveal the relationship between the contact area and  $F_N$  (13-15 from [9]). By assuming perfectly smooth asperities, with radii of curvature from micrometers all the way down to nanometers, continuum mechanics can be used to predict the deformation of asperities as normal force is applied. A model for non-adhesive contact between homogenous, isotropic, linear elastic spheres was first developed by Hertz (17 from [9]), which predicted  $A_{\text{asp}} \propto F_N^{2/3}$ . Later adhesion effects were included in a number of subsequent models, including Maugis-Dugdale theory (18 from [9]), which also predicts a sublinear relationship between  $A_{\text{asp}}$  and  $F_N$ . Thus, the common feature of all single-asperity theories is that  $A_{\text{asp}}$  is a sublinear function of  $F_N$ , leading to a similar sublinear relationship for  $F_{\text{fric}}(F_N)$ , which fails to align with the macroscale observations modelled by Amontons' law (eq. (1.1)).

A variety of multiasperity theories has attempted to combine single asperity mechanics by statistical modelling of the asperity height and spatial distributions [11]. This has led to ... a linear relationship between  $A_{\text{asp}}$  and  $F_N$ . Unfortunately, these results are restricted in terms of the magnitude of the load and contact area, where multiasperity contact models based on the original ideas of Greenwood and Williamson [12] only predicts linearity at vanishing low loads, or Persson [13] which works for more reasonable loads but only up to 10-15 % of the macroscale contact area. However, as the load is further increased all multiasperity models predict the contact area to fall into the sublinear dependency of normal force as seen for single asperity theories [11].

### 1.1.3 Nanoscale - Atomic scale

Going from a micro- to nanoscale, on the order of  $10^{-9}$  meter, it has been predicted that continuum mechanics will break down [14] due to the discreteness of individual atoms. Note that atom spacing lies in the domain of a few ångströms Å ( $10^{-10}$  m) and thus we take the so-called corresponding atomic-scale to be a part of the nanoscale regime. In a numerical study by Mo et al. [9] (considering asperity radii of 5-30 nm) it has been shown that the asperity area  $A_{\text{asp}}$ , defined by the circumference of the apparent asperity contact zone, is in fact sublinear with  $F_N$ . This is accommodated by the observation that not all atoms within the circumference make chemical contact with the substrate. By modelling the real area  $A_{\text{real}} = N A_{\text{atom}}$ , where  $N$  is the amount of atoms within the range of chemical interaction range and  $A_{\text{atom}}$  is the associated atom surface area, they found a consistent linear relationship between friction and the real contact area. Without adhesive forces this lead to a similar linear relationship  $F_{\text{fric}} \propto F_N$ , while adding van der Waals adhesion to the simulation gave a sublinear relationship, even though the  $F_{\text{fric}} \propto A_{\text{real}}$  was maintained.

This result emphasizes that contact area is still expected to be play a major role on the nanoscale for asperity theory. It is simply the definition of contact area that undergoes a change when transitioning from micro- to nanoscale. However, considering the simulation setup of our numerical study, a flat sheet on a flat substrate, it is unfounded to rely on asperity theories. With no asperities present it is unknown (I could not find any articles on contact area for nanoflakes) whether the real contact area continue to be dominant part of the friction mechanism at play. Before diving into alternative theoretical approaches to address this issue we point out that we might in fact be able to introduce an ensemble of asperities through a strategic combination of kirigami inspired cuts and stretching of the sheet. Hence, we might hypothesize that such a transition will contribute to significant change in the governing mechanism of friction in the system which we attempt to optimize for

certain properties.

In the lack of noteworthy structural asperities on, the friction can instead be modelled as a consequence of the rough potential of the atomic landscape. A series of models builds on this idea by considering different ways for the atoms to interact interatomic, with the moving body and the substrate surface. In figure 1.2 three major models 1D models is displayed. The time-honored Prandtl-Tomlinson (PT) model describes a point-like tip sliding over a space-periodic fixed crystalline surface with a harmonic coupling to the *moving body*. This is analog to that of an experimental cantilever (experimental name). Further extensions was added in the Frenkel-Kontorova (FK) model by substituting the tip with a chain of harmonic coupled atoms dragged from the end (I am not sure that the figure is correct here by drawing a spring), and finally combined in the Frenkel-Kontorova-Tomlinson (FKT) with the addition of a harmonic coupling between the chain and the moving body.

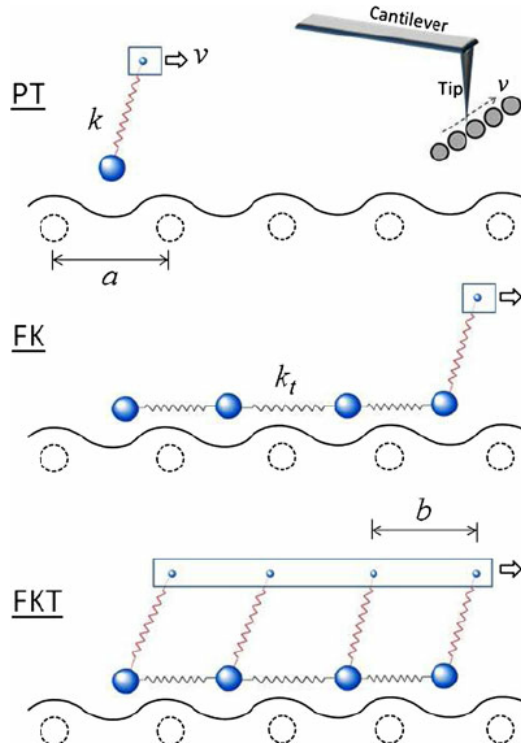


**Figure 1.2:** Temporary figure from [https://www.researchgate.net/figure/Illustrations-of-the-1D-PT-FK-and-FKT-models-Large/fig1\\_257670317](https://www.researchgate.net/figure/Illustrations-of-the-1D-PT-FK-and-FKT-models-Large/fig1_257670317)

### 1.1.3.1 Frenkel-Kontorova

The standard Frenkel-Kontorova (FK) model consists of a 1D chain of  $N$  classical particles of equal mass, representing atoms, interacting via harmonic forces and moving in a sinusoidal potential as sketched in figure 1.3. The hamiltonian is

$$H = \sum_{i=1}^N \left[ \frac{p_i^2}{2m} + \frac{1}{2} K(x_{i+1} - x_i - a_c)^2 + \frac{1}{2} U_0 \cos\left(\frac{2\pi x_i}{a_b}\right) \right], \quad (1.2)$$

where the atoms are labelled sequentially  $i = 1, \dots, N$ . The first term  $p_i^2/2m$  represents the kinetic energy with momentum  $p_i$  and mass  $m$ . Often the effects of inertia are neglected, referred to as the static FK model, while the inclusion, as shown in eq. (1.2), is known as the dynamic FK model [15]. The next term describes the harmonic interaction with elastic constant  $K$ , nearest neighbour distance  $\Delta x = x_{i+1} - x_i$  and corresponding nearest neighbour equilibrium distance  $a_c$ . The final term represents the periodic substrate potential (external potential on site) with amplitude  $U_0$  and period  $a_b$ . Different boundary choices can be made where both free

ends nad periodic conditions gives reasonable results. The choice of fixed ends however makes the chain incapable of sliding.

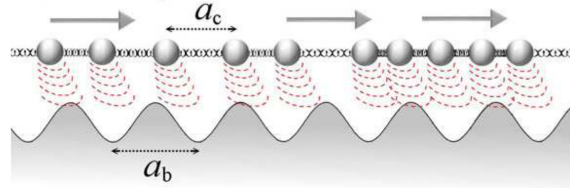


**Figure 1.** A sketch of the FK model, showing the two competing lengths: the average interparticle spacing and the lattice periodicity of the substrate.

**Figure 1.3:** [Temporary figure from [6]]

To probe static friction one can apply an external force which increases adiabatically until sliding accours. This corresponds to the static FK model and it turns out that the sliding properties are entirely governed by its topological excitations referred to as so-called *kinks* and *antikinks*

**Commensurability** We can describe the frictional behvaiour in terms of commensurability, that is, how well the spacing of the atoms match the periodic substrate potential. We describe this by the length ratio  $\theta = a_b/a_c = N/M$  where  $M$  denotes the number of minemas in the potential (within the length of the chain). A rational number for  $\theta$  means that we can align the atoms in the chain perfectly with the minemas, without stretching the chain, corresponding to a *commensurate* case. If  $\theta$  is irrational the chain and substrate cannot fully align, and we denote this as being *incommensurate*.

We begin with the simplest commensurate case of  $\theta = 1$  where the spacing of the atoms matches perfectly the substrate potential periodicity, i.e.  $a_c = a_b$ ,  $N = M$ . The ground state (GS) is the configuration where each atom fits in one of the substrate minema. By adding an extra atom we would effectively shift over some atoms, away from these ideal state, giving rise to a kink excitation, i.e. two atoms will have to share the same potential corrugation as sketched in figure 1.5. On the other hand, removing an atom from the chain results in a antikink excitation where one potential corrugation will be left “atomless”. In order to reach a local minimum the kink (antikink) will expand in space over a finite length such that the chain undertakes a local compression (expansion). When applying a tangential force to the chain it is much easier for a kink to move along the chain than it is for the non-excited atoms since the activation energy  $\epsilon_{PN}$  for a kink displacement is systematically smaller (often much smaller) than the potential barrier  $U_0$ . Thus, the motion of kinks (antikinks), i.e. the displacement of extra atoms (atom vacancies), is represententing the fundamental mechanism for mass transport. These displacements is responsible for the mobility, diffusivity and conductivity within this model.

In the ideal zero temperature commensurable case with an adiabatical increase in force, all atoms would be put into an accelerating motion as soon the lowest energy  $NU_0$  is present. However, in reality any thermal excitation would excite the system before this point is reached by the creation of kink-antikink pairs that would travel down the chain. For a chain of finite length these often accrour at the end of the chain running in opposite direction. As a kink travels down the chain the atoms is advanced by one atom spacing  $a_b$  along the substrate potential. This cascade of kink-antikink exications is shown in figure 1.4

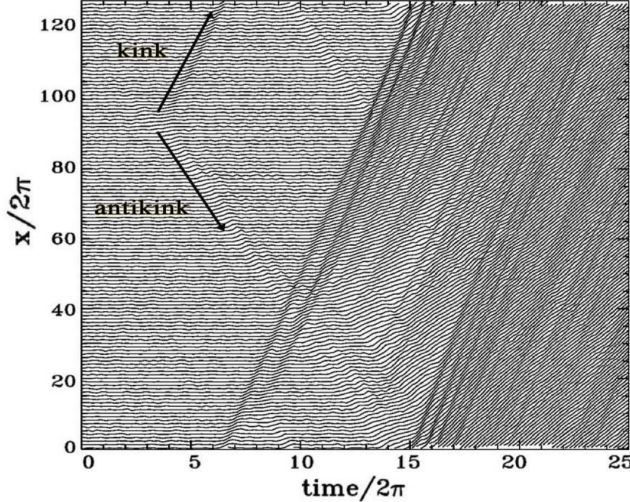


**Figure 2.** Time dependence of the atomic trajectories for the fully matched ( $\theta = 1$ ) FK model at the (low-temperature) onset of depinning. Motion starts with the nucleation of a kink-antikink pair. The kink and the antikink depart in opposite directions cross the periodic boundary conditions, and collide quasielastically. A second kink-antikink pair forms in the wake of the initial kink. Further kink-antikink pairs are generated, with an avalanche-like increase of the kink-antikink concentration, eventually leading to a sliding state. Adapted from Ref. [21], Copyright (1997) by The American Physical Society.

**Figure 1.4:** **Temporary** figure from [6]

For the 2D case where an island is deposited on a surface, in our case the graphene sheet on the Si substrate, we generally also expect the sliding to be initiated by kink-antikink pairs at the boundary.

For the case of incommensurability, i.e.  $\theta = a_b/a_c$  is irrational, the GS is characterized by a sort of ‘‘staircase’’ deformation. That is, the chain will exhibit regular periods of regions where the chain is slightly compressed (expanded) to match the substrate potential, separated by kinks (antikinks), where the increased stress is eventually released through a localized expansion (compression) as illustrated in figure 1.5 Go though this again and make sure that I got the compression expansion directions rihgt....



**Figure 1.5:** **Temporary** figure from [urlhttp://www.iop.kiev.ua/~obraun/myreprints/surveyfk.pdf](http://www.iop.kiev.ua/~obraun/myreprints/surveyfk.pdf) p. 14. Incommensurable case ( $\theta = ?$ ) where atoms sits slightly closer than otherwise dictated by the substrate potential for which this regularly result in a kink here seen as the presence of two atoms closeæy together in on of the potential wells.

The incommensurable FK model contains a critical elastic constant  $K_c$ , such that for  $K > K_c$  the static friction  $F_s$  drops to zero, making the chain able to initiate a slide at no energy cost, while the low-velocity kinetic friction is dramatically reduced. This can be explained by the fact that the displacement accouring in the incommensurable case will yield just as many atoms climbing up a corrugation as there are atoms climbing down. For an infinite chain this will exactly balance the forces making it non-resistant to sliding. Generally, incommensurability guarantees that the total energy (for  $T = 0$ ) is independent of the relative position to the potential. However, when sliding freely a single atom will eventually occupy a maximum of the potential. When increasing the potential magnitude  $U_0$  or softning the chain stiffness, lowering  $K$ , the possibility to occupy such a maximum is no longer present. This marks the so-called Aubry transition at the critical elasic constant

$K = K_c(U_0, \theta)$  where the chain goes from a free sliding to a *pinned state* with a nonzero static friction.  $K_c$  is a discontinuous function of the ratio  $\theta$ , due to the reliance on irrational numbers for incommensurability. The minimal value  $K_c \simeq 1.0291926$  in units  $[2U_0(\pi/a_b)^2]$  is achieved for the golden-mean ratio  $\theta = (1 + \sqrt{5}/2)$ . Notice that the pinning is provided despite translational invariance due to the inaccessibility to move past the energy barrier which act as dynamical constraint. The Aubry transistion can be invistigated as a first-order phase transistion for which power laws can be defined for the order parameter. This is beyond the scope of this thesis as we merely are going to point to the FK model for the understanding of stick-slip behvaiour and the concept of commensurability.

The phenonema of non-pinned configurations is named *superlubricity* in tribological context. Despite the misleadning name this referses to the case where the static friction is zero while the kinetic friction is nonzero but reduced. For the case of a 2D sheet it is possible to alter the commensurability by changing the orientation of the sheet relative to the substrate. This has been shown for a graphene flake (single layer) sliding over a graphite surface (multiple layers) [16]. In figure 1.6 we see how the friction depends on the relative orientatin between the sheet and substrate.

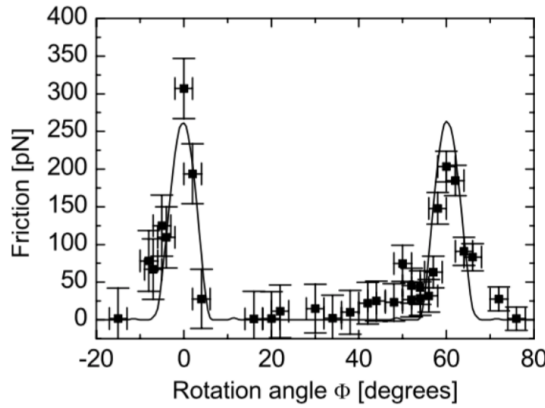


Fig. 6. Average friction force versus rotation angle  $\Phi$  of the graphite sample around an axis normal to the sample surface. Two narrow peaks of high friction are observed at  $0^\circ$  and  $61^\circ$ , respectively. Between these peaks a wide angular range with ultra-low friction, close the detection limit of the instrument, is found. The first peak has a maximum friction force of  $306 \pm 40$  pN, and the second peak has a maximum of  $203 \pm 20$  pN. The curve through the data points shows results from a Tomlinson model for a symmetric 96-atom graphite flake sliding over the graphite surface (for details about the calculation see [39]).

**Figure 1.6:** [Temporary] figure from [16] showing superlubricity for incommensurable orientations between graphene and graphite. [temporary]

**Kinetic friction** In the FK model the kinetic friction is primarily caused by resonance between the sliding induced vibrations and phonon modes in the chain [15]. When all atoms are sliding rigidly width center of mass velocity  $v_{CM}$  the atoms will pass the potential maxima with the so-called *washboard frequency*  $\Omega = 2\pi v_{CM}/a_b$ . For a weak coupling between the chain and the potential we can use the zero potential case as an approximation for which the known dispersion relation for the 1D harmonic chain is given [Kittel]

$$\omega_k = \sqrt{\frac{4K}{m}} \left| \sin \left( \frac{k}{2} \right) \right|,$$

where  $\omega_k$  is the phonon frequency and  $k = 2\pi i/N$  the wavenumber with  $i \in [N/2, N/2]$ . Strong resonance will accour if  $\Omega$  is close to the frequency of the phonon modes  $\omega_q$  in the chain with wavenumber  $q = 2\pi a_c/a_b = 2\pi\theta^{-1}$

or its harmonics  $nq$  for  $n = 1, 2, 3, \dots$  [17]. Thus, we can approximate the resonance speed as

$$\begin{aligned} n\Omega &\sim \omega_{nq} \\ n\frac{2\pi v_{CM}}{a_b} &\sim 2\sqrt{\frac{K}{m}} \left| \sin\left(\frac{2n\pi\theta^{-1}}{2}\right) \right| \\ v_{CM} &\sim \frac{\sin(n\pi\theta^{-1})}{n\pi} \sqrt{\frac{Ka_b^2}{m}}. \end{aligned}$$

When the chain slides with a velocity around resonance speed, the washboard frequency can excite acoustic phonons which will dissipate to other phonon modes as well. At zero temperature the energy will transform back and forth between internal degrees of freedom and center of mass movement of the chain. Hence, at zero temperature this will indeed speed up the translation decay (decay is synonymous for translational movement right?). However, for the more realistic case of non-zero temperature the substrate serves as a thermostat for which energy will dissipate from the chain to the substrate degrees of freedom giving rise to kinetic friction. On the other hand, this predicts that certain sliding speed, which does not induce phonon resonance, will be subject to extremely low kinetic friction. This is strongly connected to the superlubricity term although this phonon dynamics is simplified in this 1D model.

A common way to model the non-zero temperature case is by the use of a Langevin thermostat, which simulates the dissipation by adding a viscous damping force and thermal fluctuations by the addition of Gaussian random forces with variance proportional to the temperature (This is covered in more details in section 1.2.3.1). In combination, this gives rise to a kinetic friction that is both velocity and temperature dependent.

By extending the FK model into 2D [15] it can be shown numerically that the friction coefficient generally increases with increasing velocity and temperature respectively.

**Smooth sliding** Find a suitable place to introduce smooth sliding. Above certain velocities the stick-slip motion disappears. [1, p. 142-ish]

### 1.1.3.2 Experimental procedures

[1]

Experimentally nanoscale friction is challenging to approach as the forces, on the scale of nano-newtons as well, is extremely small. Additionally surface topography is not easily viewed. On the other side simulations provide full transparency regarding information of the physical structure of the sample along with forces, velocities and temperature. However, in order to compare numerical results the experimental procedures is most often mirrored in simulations. Thus it is beneficial to address the most common experimental techniques when designing a simulation.

**Scanning Probe Microscopy** Scanning probe microscopy (SPM) includes a variety of experimental methods which is used to examine surfaces with atomic resolution [18, p. 6-]. This was originally developed for surface topography imaging, but today it plays a crucial role in nanoscale science as it is used for probe-sampling regarding tribological, electronic, magnetic, biological and chemical character. The family of methods involving the measurement of forces is generally referred to as *scanning force microscopies* (SFM).

One such method arose from the *atomic force microscope*, which consist of a sharp micro-fabricated tip attached to a cantilever force sensor, usually with a sensitivity below 1 nN. The force is measured by recording the bending of the cantilever, either as a change in electrical conduction or more commonly, by a light beam reflected from the back of the cantilever into a photodetector [1]. By adjusting the tip-sample height to keep a constant normal force while scanning across the surface this can be used to produce a surface topography map. By tapping the material (dynamic force microscopy) with sinusoidally vibrated tip the effects from friction and other disturbing forces can be minimized in order to produce a clear image (include example, preferable of graphene). However, when scanning perpendicularly to the cantilever axis one is also able to measure the frictional force as torsion of the cantilever. By having four quadrants in the photodetector (as shown in figure 1.7), one can simultaneously measure the normal force and friction force as the probe scans across the surface.

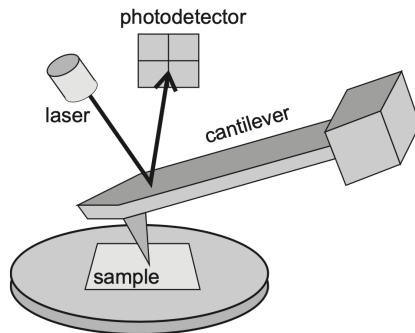


Figure 17.1 Schematic diagram of a beam-deflection atomic force microscope.

**Figure 1.7:** **Temporary** figure from [1, p. 184]

This can also be used to drag a nanoflake as done by Dienwiebel et al. [16] (earlier referenced), where a graphene flake was attached to a FFM tip and dragged across graphite.

**Surface Force Apparatus (SFA)** Is this the one where two surfaces slides in opposite direction (at least that is the common MD way I see it.)

### 1.1.3.3 (summary of) Expected frictional properties

The setup of our simulation is most reminiscent of a graphene flake sliding on a substrate. This has been studied numerically in molecular dynamic simulations by Zhu and Li [19, 2018] for a graphene flake on a gold substrate and by Zhang et al. [20](2019) on a diamond substrate, and in a tight-binding simulation by Bonelli et al. [21](2009) for graphene on graphite. Experimental studies of a graphene flake attached to a AFM is done by Dienwiebel et al. [16, 2005] and Feng et al. [22, 2013] sliding on graphite, but these are mainly concerned with superlubricity as a function of flake orientation commensurability.

In our study we simulate a graphene flake on a silicon substrate which deviates slightly from the above-mentioned reference. Additionally, the normal force is only applied to the ends of the sheet. Obviously stretching and cutting the sheet will separate our study dramatically from the references, but we aim to compare the frictional properties to the reference before applying stretch or cuts.

Qualitatively we have the following expectations for the unstretched and non-cut graphene sheet.

#### Qualitatively

1. Stick slip: Generally expect to see periodic stick-slip motion with a period matching the lattice constant(s) involved [9]. This was both present in the MD simulations [19], [20] and in the experiment by [16]. In AFM and SFA experiments, the stick-slip motion tends to transition into smooth sliding when the speed exceeds  $\sim 1\mu \text{ m/s}$  while in MD modelling the same transition is observed in the  $\sim 1\text{m/s}$  region [6]. This order of magnitude discrepancy has been largely discussed in connection to simplifying assumptions in MD simulations. Bonelli et al. [21] found that the stick-slip behaviour was present when the cantilever-tip-flake coupling was done with a relatively soft springs in contrast to hard springs which inhibited it.
2. Static friction: As highlighted in the FK model static friction will be sensitive to commensurability, which will additionally be affected by flake size. Reguzzoni and Righi [23] have shown that the effective commensurability will increase drastically below a critical flake radius on the order of  $10 \text{ \AA}$ . Macroscopically we expect to see a logarithmic increase in friction with time [8], and hence due to the short time-span of the static contact before dragging, it is not easy to estimate whether a significant static friction peak will be found.
3. Orientation: As predicted by the FK model and confirmed both numerically [19], [20] and experimentally [16], [22] we expect to see a dependence from orientation on the friction force due to changing commensurability. Zhu and Li [19] (gold substrate) reported the highest friction when sliding along the armchair

direction, while Zhang et al. [20] (diamond substrate) found the zigzag-direction to give the highest friction force along the zigzag direction (also the most evident stick-slip behaviour).

**Table 1.1:** Quantitative nano friction dependence on various variables.

Variable	Dependency	Numerical studies	Experimental
Normal force $F_N$	$F_f$ increasing $F_N$	MD simulations of amorphous carbon asperity on diamond substrate suggest a linear relationship to $F_f \propto F_N$ for nonadhesive contact and sublinear with van der waals adhesive forces [9]. Graphene flake?	The general trend observed in AFM nanoscale friction is that friction force increase with normal load [1, p.200]. Various trends have been observed from linear to power trends.
Velocity $v$	$F_f \propto \ln v$		
Temperature $T$	$F_f \propto 1/T$		
Real contact area $A$	$F_f \propto A$		

**Table 1.2:** Quantitative nano friction dependence on various variables.

Variable	Dependency	Numerical studies	Experimental
Normal force $F_N$	$F_f$ increasing $F_N$	MD simulations of amorphous carbon asperity on diamond substrate suggest a linear relationship to $F_f \propto F_N$ for nonadhesive contact and sublinear with van der waals adhesive forces [9]. Graphene flake?	The general trend observed in AFM nanoscale friction is that friction force increase with normal load [1, p.200]. Various trends have been observed from linear to power trends.
Velocity $v$	$F_f \propto \ln v$		
Temperature $T$	$F_f \propto 1/T$		
Real contact area $A$	$F_f \propto A$		

## 1.2 Molecular Dynamics

Maybe also ‘‘Computer Simulations 7 of Nanometer-Scale Indentation and Friction’’ from [18]

Read [6][p. 18]

A promising compromise could possibly be provided by the so-called reactive potentials [120–122], capable of describing some chemical reactions, including interface wear with satisfactory computational efficiency in large-scale atomic simulations, compared to semi-empirical and first-principles approaches. [6]

- MD simulation (classical or ab initio)
- Basics of classical MD simulations: Integration and stuff
- Ab initio simulation (quantum mechanics, solving schrödinger)

### 1.2.1 Potentials

The choices of potentials used in the MD simulation is mainly based on the on [24] which have a somewhat similar MD friction simulation, the difference being that they impose a Si-tip on the graphene sheet supported by a Si-substrate where we impose drag the whole sheet upon the substrate. Nonetheless this serves as a good anchor for the methodology of the setup. The covalent bonds of C-C in graphene and Si-Si in the substrate is

described by the Tersoff and Stillinger–Weber potentials, respectively. A typical 12-6 Lennard–Jones potential is used to describe the van der Waals adhesive interaction between graphene and the substrate.

### 1.2.1.1 General formulation of potentials (?)

On a general note we can generalize the n-body potential as the expansion in orders of participating atoms as

$$E = \sum_i V_1(\mathbf{r}_i) + \sum_{\substack{i,j \\ i < j}} V_2(\mathbf{r}_i, \mathbf{r}_j) + \sum_{\substack{i,j,k \\ i < j < k}} V_3(\mathbf{r}_i, \mathbf{r}_j, \mathbf{r}_k) + \dots$$

where  $\mathbf{r}_n$  is the position of the  $n$ th particle and  $V_m$  is called an  $m$ -body potential [25]. The first one-body term corresponds to an external potential, followed by the two-body term, the three-body term and so on. The simplest model that includes particle interaction is the pair potential truncating the expansion after the two-body term. A general feature of the pair potentials is that they favor close-packed structures which is unsuited to describe covalent bonds that take more open structures. In particular, pair potentials are completely inapplicable to strongly covalent systems such as semiconductors [25]. In order to accommodate the description of covalent bonds the natural step is thus to include the next step of the expansion, the three-body terms, as we will see for the modeling of the graphene sheet C-C bonds and the Silicon sheet Si-Si bonds. For the interaction between the sheet and the substrate we can notes med a Lennard Jones pair potential describing the non-bonded van der Waals interaction.

### 1.2.1.2 Lennard Jones

This sections is based on [[26], [27], [28]].

The Lennard-Jones (LJ) model is probably one of the most famous pair potentials used in MD simulations. LJ models the potential energy between two non-bonding atoms based solely on interatomic distance  $r$ . The model accounts for attractive forces arising from dipole-dipole, dipole-induced dipole and London interactions, and repulsive forces that capture the hard core (is this safe to say?) of overlapping wave functions at small distances. Thus it is assumed neutrally charged atoms and was originally proposed for noble gases. The classical 12-6 version of the model (referring to the power law of the repulsive and attractive forces respectively) reads

$$E = 4\epsilon \left[ \left( \frac{\sigma}{r} \right)^{12} - \left( \frac{\sigma}{r} \right)^6 \right], \quad r < r_c, \quad (1.3)$$

where  $r$  is the interatomic distance with cut-off  $r_c$ ,  $\epsilon$  is the depth of the potential well and  $\sigma$  the distance where the potential is zero. By solving for the potential minimum ( $dE/dr = 0$ ) we find the equilibrium distance to be  $r_0 = \sigma 2^{1/6}$ . This makes for an even clear interpretation of  $\sigma$  which effectively sets the equilibrium distance between atoms, i.e. the dividing line for which the net force is repulsive or attractive. While the LJ model in many ways is an oversimplified model that is insufficient in its description of ... (get source and concrete examples) it is commonly used as a model for intermaterial interactions (between moving object and substrate) in friction studies [[24], [29], [3]].

### 1.2.1.3 Stillinger weber

This section is based on [[30], [31]]

The stillinger weber potential takes the form of a three body potential

$$E = \sum_i \sum_{j>i} \phi_2(r_{ij}) + \sum_i \sum_{j \neq i} \sum_{k>j} \phi_3(r_{ij}, r_{ik}, \theta_{ijk}),$$

where  $r_{ij}$  denotes the distance between atom  $i$  and  $j$  and  $\theta_{ijk}$  the angle between bond  $ij$  and  $jk$ . The summations is over all neighbours  $j$  and  $k$  of atom  $i$  within a cut-off distance  $r = a\sigma$ .

The two-body term  $\phi_2$  builds from the LJ model with the addition of an exponential cutoff term

$$\phi_2(r_{ij}) = A_{ij}\epsilon_{ij} \left[ B_{ij} \left( \frac{\sigma_{ij}}{r_{ij}} \right)^{p_{ij}} - \left( \frac{\sigma_{ij}}{r_{ij}} \right)^{q_{ij}} \right] \exp\left(-\frac{\sigma_{ij}}{r_{ij} - a_{ij}\sigma_{ij}}\right). \quad (1.4)$$

The model parameters  $A$ ,  $\epsilon$ ,  $B$ ,  $\sigma$ ,  $p$ ,  $q$  and  $a$  comes with  $i, j$  indices to indicate that theese parameters should be specified for each unique pair of atom types. However, in our case we will only provide a single value for each model parameter as we are exclusively dealing with Si-Si bonds. We see that the first term in eq. (1.4) is reminiscent of the LJ model in eq. (1.3) while the last term effectively drives the potential to zero at  $r = a\sigma$ , which is thus the chosen cut-off distance for the potential evaluation. With the model parameters for the Si-Si modelling (see table 1.3) the cut-off becomes  $\sim 3.8 \text{ \AA}$ .

The three body term includes an angle dependency as

$$\phi_3(r_{ij}, r_{ik}, \theta_{ijk}) = \lambda_{ijk} \epsilon_{ijk} \left[ \cos \theta_{ijk} - \cos \theta_{0,ijk} \right]^2 \exp\left(\frac{\gamma_{ij}\sigma_{ij}}{r_{ij} - a_{ij}\sigma_{ij}}\right) \exp\left(\frac{\gamma_{ik}\sigma_{ik}}{r_{ik} - a_{ik}\sigma_{ik}}\right), \quad (1.5)$$

where  $\theta_{0,ijk}$  is the equilibrium angle. The first term of eq. (1.5) includes an angle dependency analog to a harmonic oscillator based on a cosine angle distance from the equilibrium angle. The final two terms act again as a cut-off function by driving the potential to zero at  $r_{ij} = a_{ij}\sigma_{ij}$  and  $r_{ik} = a_{ik}\sigma_{ik}$  respectively.

The parameters used for the Si-Si bond modeling is displayed in table 1.3 along with an interpretation of each model parameter.

**Table 1.3:** Parameters for the stilliner weber potential used for intermolecular interactions in the silicon substrate.

Parameter	Value	Description
$\epsilon$	2.1683	Individual depth of the potential well for each atom type pair/tiplets.
$\sigma$	2.0951	Distance for which the individual pair interactions has zero potential (analog to the LJ model).
$a$	1.80	The individual cut-off distance for each atom type pair.
$\lambda$	21.0	The overall depth of the three-body potential well.
$\gamma$	1.20	The shape of the three-body cut-off terms.
$\cos(\theta_0)$	-1/3	Cosine of equilibrium angle.
$A$	7.049556277	The overall depth of the two-body potential well.
$B$	0.6022245584	Scales the repulsion part of the two-body term.
$p$	4.0	The power dependency for the repulsion part of the two-body term.
$q$	0.0	The power dependency for the attraction part of the two-body term.
tol	0.0	LAMMPS: Option to define a different cut-off than the theoretical of $r = a\sigma$ . tol = 0 refers to the theoretical being used.

#### 1.2.1.4 Tersoff

This section is based on [[32], [25]].

The tersoff potential abandon the idea of a general  $n$ -body form and attempts instead to build the model on a more physics informed approach; The more neighbours an atom has the weaker the bonds will be. Thus it introduces the bond order (bond strenght), that is environment specific and decrease with increasing bond coordination (number of neighbours for a given atom). The potential energy is taken to have the form

$$E = \sum_i E_i = \frac{1}{2} \sum_{i \neq j} V_{ij},$$

$$V_{ij} = f_C(r_{ij}) [f_R(r_{ij}) + b_{ij}f_A(r_{ij})],$$

where the total potential energy is decomposed into a bond energy  $V_{ij}$ . The indices  $i$  and  $j$  run over the atoms of the system with  $r_{ij}$  denoting the distance between atom  $i$  and  $j$ . Notice that the sum includes all combinations of  $i, j$  where  $i \neq j$  meaning that the same bond is double counted which is the reason for the additional factor 1/2. The reasoning behind comes from the asymmetry of the bond order  $b_{ij} \neq b_{ji}$  leading to a

$V_{ij} \neq V_{ji}$ . The bond energy is composed of a repulsive term  $f_R$ , arising from overlapping wave functions, and an attractive term  $f_A$  associated with bonding.  $f_c$  is simply a smooth cut-off function to increase computational efficiency.  $b_{ij}$  represent the bond order, i.e. the strength of the bonds, which depends inversely on the number of bonds, the bond angles ( $\theta_{ijk}$ ) and optionally the relative bonds lengths ( $r_{ij}, r_{jk}$ ). Notice that an additional cut-off term  $a_{ij}$  was originally multiplied to  $f_R$  as a way of including terms that limit the range of the interactions to the first neighbour shell. These kind of limitations is already included in  $b_{ij}$  for the attractive term  $f_A$  but is often omitted for the repulsive term  $f_R$ , and we do so to by setting  $a_{ij} = 1$ .

The cut-off function  $f_C$  goes from 1 to 0 over a small interval range  $R \pm D$  as

$$f_C(r) = \begin{cases} 1 & r < R - D \\ \frac{1}{2} - \frac{1}{2} \sin\left(\frac{\pi}{2} \frac{r-R}{D}\right) & R - D < r < R + D \\ 0 & r > R + D \end{cases}$$

which is continuous and differentiable for all  $r$ .  $R$  is usually chosen to include only the first neighbour shell. The repulsive and attractive terms  $f_R$  and  $f_A$  is modelled as an exponential function, similar to a morse potential,

$$\begin{aligned} f_R(r) &= A \exp(-\lambda_1 r), \\ f_A(r) &= -B \exp(-\lambda_2 r). \end{aligned}$$

The novel feature of the model lies in modeling of the bond order  $b_{ij}$  which includes three-body interactions by summing over a third atom  $k \neq i, j$  within the cut-off  $r_{ik} < R + D$  as shown in the following.

$$b_{ij} = (1 + \beta^n \zeta_{ij}^n)^{-\frac{1}{2n}} \quad (1.6)$$

$$\zeta_{ij} = \sum_{k \neq i, j} f_C(r_{ik}) g(\theta_{ijk}(r_{ij}, r_{ik})) \exp(\lambda_3^m (r_{ij} - r_{ik})^m) \quad (1.7)$$

$$g(\theta) = \gamma_{ijk} \left( 1 + \frac{c^2}{d^2} - \frac{c^2}{[d^2 + (\cos \theta - \cos \theta_0)^2]} \right). \quad (1.8)$$

In eq. (1.8)  $\zeta_{i,j}$  is an effective coordination and  $g(\theta)$  captures angle dependency as it is minimized at the equilibrium angle  $\theta = \theta_0$ .

The parameters used to model the graphene C-C bonds is summarized in table 1.4

**Table 1.4:** Parameters for the tersoff potential used for intermolecular interations in the graphene sheet

Parameter	Value	Description
$m$	3.0	Default (not used since $\lambda_3 = 0$ )
$\gamma$	1.0	...
$\lambda_3$	$0.0 \text{ \AA}^{-1}$	...
$c$	$3.8049 \times 10^4$	Strength of the angular effect
$d$	4.3484	Determines the “sharpness” of the angular dependency
$\cos(\theta_0)$	-0.57058	Cosine of the equilibrium angle
$n$	0.72751	Power law exponent for the bond order dependency
$\beta$	$1.5724 \times 10^{-7}$	...
$\lambda_2$	$2.2119 \text{ \AA}^{-1}$	Decay of repulsion potential term
$B$	346.74 eV	Attractive potential term minimum at core ( $r_{ij} = 0$ ).
$R$	1.95 Å	Center distance for cut-off
$D$	0.15 Å	Thickness of cut-off layers
$\lambda_1$	$3.4879 \text{ \AA}^{-1}$	Decay of repulsion potential term
$A$	1393.6 eV	Repulsion potential term at core ( $r_{ij} = 0$ )

## 1.2.2 Integration

Having defined a system of particles governed by interatomic potentials we need to move the system forward in time. By solving Newtons equations of motion we effectively do so by sampling the microcanonical ensemble characterized by a constant number of particles  $N$ , volume  $V$  and energy  $E$ , hence denoted NVE. Newtons equaitons of motion read

$$m_i \frac{d^2 \mathbf{r}_i}{dt^2} = \mathbf{F}_i = -\nabla U_i \quad (1.9)$$

where  $i$  is the particle index and  $m_i$  its mass,  $\mathbf{r}_i = (x_i, y_i, z_i)$  the position,  $t$  is time,  $\nabla_i = (\frac{\partial}{\partial x_i}, \frac{\partial}{\partial y_i}, \frac{\partial}{\partial z_i})$  and  $U_i$  the potential energy. In system the potential energy is a function of the particle positions of nearby particles depending on the specefic potential in use. Since the forces defined by the potentials is conservative we expect the energy of the solution to be conserved. We redefine eq. (1.9) in terms of two coupled first order differential equations

$$\dot{\mathbf{v}}_i(t) = \frac{\mathbf{F}}{m_i}, \quad \dot{\mathbf{r}}_i(t) = \mathbf{v}_i(t), \quad (1.10)$$

where  $\dot{x} = dx/dt$  (Newton's notation) and  $\mathbf{v} = (v_x, v_y, v_z)$  is velocity. Numerically we can solve the coupled equations (eq .(1.10)) by integrating over discrete timnesteps. That is, we discretize the solution into temporal steps  $t_k = t_0 + k \cdot \Delta t$  with time-step  $\Delta t$ .

### 1.2.2.1 Velocity Verlet

A common algorithm to integrate Newtons equation of motion (as formulated in eq. (1.10)) is the *velocity verlet*. We can derive the algorithm by the use of Taylor expansions. We begin by expanding the next-step position vector  $\mathbf{r}_i(t + \Delta t)$  at time  $t$

$$\mathbf{r}_i(t + \Delta t) = \mathbf{r}_i(t) + \dot{\mathbf{r}}_i(t)\Delta t + \frac{\ddot{\mathbf{r}}_i(t)}{2}\Delta t^2 + \mathcal{O}(\Delta t^3), \quad (1.11)$$

where  $\ddot{\mathbf{r}} = d^2\mathbf{r}/dt^2$  and  $\Delta t^n$  is simply the relaxed notation for  $(\Delta t)^n$ . Similar we take the expansions of the next-step velocity vector  $\mathbf{v}_i(t + \Delta t)$  at time  $t$

$$\mathbf{v}_i(t + \Delta t) = \mathbf{v}_i(t) + \dot{\mathbf{v}}_i(t)\Delta t + \frac{\ddot{\mathbf{v}}_i(t)}{2}\Delta t^2 + \mathcal{O}(\Delta t^3). \quad (1.12)$$

Finnally, by taking the expansion of  $\dot{\mathbf{v}}_i(t + \Delta t)$  we can eliminate the  $\ddot{\mathbf{v}}_i$ -term in eq. (1.12) and simplify it as shown in the following.

$$\begin{aligned} \dot{\mathbf{v}}_i(t + \Delta t) &= \dot{\mathbf{v}}_i(t) + \ddot{\mathbf{v}}_i(t)\Delta t + \mathcal{O}(\Delta t^2) \\ \frac{\ddot{\mathbf{v}}_i(t)}{2}\Delta t^2 &= \frac{\Delta t}{2} \left( \dot{\mathbf{v}}_i(t + \Delta t) - \dot{\mathbf{v}}_i(t) \right) + \mathcal{O}(\Delta t^3) \\ &\Downarrow \\ \mathbf{v}_i(t + \Delta t) &= \mathbf{v}_i(t) + \dot{\mathbf{v}}_i(t)\Delta t + \frac{\Delta t}{2} \left( \dot{\mathbf{v}}_i(t + \Delta t) - \dot{\mathbf{v}}_i(t) \right) + \mathcal{O}(\Delta t^3) \\ &= \mathbf{v}_i(t) + \frac{\Delta t}{2} \left( \dot{\mathbf{v}}_i(t) + \dot{\mathbf{v}}_i(t + \Delta t) \right) + \mathcal{O}(\Delta t^3). \end{aligned} \quad (1.13)$$

By combining eq. (1.11) and eq. (1.13) and using Newton's second equation  $\dot{\mathbf{v}} = \mathbf{F}_i(t)/m_i$  and  $\mathbf{v} = \dot{\mathbf{r}}$  we arrive at the final scheme

$$\begin{aligned} \mathbf{r}_i(t + \Delta t) &= \mathbf{r}_i(t) + \mathbf{v}_i(t)\Delta t + \frac{\mathbf{F}_i(t)}{2m_i}\Delta t^2 + \mathcal{O}(\Delta t^3), \\ \mathbf{v}_i(t + \Delta t) &= \mathbf{v}_i(t) + \frac{\mathbf{F}_i(t) + \mathbf{F}_i(t + \Delta t)}{2m_i}\Delta t + \mathcal{O}(\Delta t^3). \end{aligned}$$

The scheme will give a local error of order  $\Delta t^3$  corresponding to a global error of  $\Delta t^2$ . One of the most popular ways to implement this numerically is as stated in the following steps.

1. Calculate  $v_{k+\frac{1}{2}} = v_k + \frac{F_k}{2m} \Delta t$ .
2. Calculate  $r_{k+1} = r_k + v_{k+\frac{1}{2}} \Delta t$ .
3. Evaluate the force  $F_{k+1} = F(r_{k+1})$ .
4. Calculate  $v_{k+1} = v_{k+\frac{1}{2}} + \frac{F_{k+1}}{2m} \Delta t$

### 1.2.3 Thermostats

As we already mentioned above in Sec. 2, any kind of sliding friction involves mechanical work, some of which is then transformed into heat (the rest going into structural transformations, wear, etc.). The heat is then transported away by phonons (and electrons in the case of metallic sliders) and eventually dissipated to the environment [6].

Likewise all excitations generated in the simulations should be allowed to propagate in the system and disperse in the bulk of both sheet and substrate. Due to small simulation size this is likely to reflect back and ‘pile up’ unphysically. Thus in order to avoid continuous heating and attain a steady state the (Joule) heat must be removed at a steady state. This is very the viscous damping of the Langevin equations enter the picture. It can be difficult to set the value  $\gamma$  for the magnitude of this damping. The unphysical introduction of heat sink can be mitigated by some modifications he mention, which is kind of next level I guess.

#### 1.2.3.1 Langevin thermostat

In order to control the temperature of the system we introduce the so-called Langevin thermostat. This is a stochastic thermostat that modifies Newton's equation of motion such that solution lies in the canonical ensemble characterized by a constant number of particles  $N$ , constant volume  $V$  and constant temperature  $T$ , hence denoted NVT. The canonical ensemble system is represented by the finite system being in contact with an infinite heat bath of temperature  $T$ . The NVT ensemble is equivalent to sampling a system in thermodynamic equilibrium where the weight of each microscopic state is given by the Boltzmann factor  $\exp[-E/(k_B T)]$ .

The Langevin equation is the modified version of Newton's second law for a Brownian particle. A Brownian particle is a small particle suspended in liquid, e.g. pollen or dust, named after Robert Brown (1773–1858) who was the first to observe its jittery motion. The Langevin equation describes this motion as the combination of viscous drag force  $-\gamma \mathbf{v}$ , where  $\gamma$  is a positive friction coefficient and  $\mathbf{v}$  the velocity vector, and a random fluctuation force  $\mathbf{R}$ . The Langevin equation reads

$$m \frac{d\mathbf{v}}{dt} = -\gamma \mathbf{v} + \mathbf{R} \quad (1.14)$$

where  $m$  is the particle mass. This effectively describes the particle of interest, the Brownian particle, as being suspended in a sea of smaller particles. The collision with these smaller particles is modelled by the drag force and the fluctuation force. We notice that if the fluctuation force is excluded eq. (1.14) becomes

$$m \frac{d\mathbf{v}}{dt} = -\gamma \mathbf{v} \quad \Rightarrow \quad \mathbf{v}_i(t) = \mathbf{v}(0) e^{-\frac{\gamma t}{m}},$$

where the solution shows that the Brownian particle will come to a complete stop after a long time  $\mathbf{v}_i(t \rightarrow \infty) \rightarrow \mathbf{0}$ . This is in violation with the equipartition theorem

$$\frac{1}{2} m \langle v^2 \rangle_{eq} = \frac{k_B T}{2},$$

and hence the fluctuation force is necessary to obtain the correct equilibrium.

The following calculations are done in one dimension in order to simplify the notation. We describe the statistical nature of the collisions as a sum of independent momentum transfers

$$\Delta P = \sum_i^N \delta p_i$$

where  $\Delta P$  denotes the change of momentum after  $N$  momentum transfers  $\delta p_i$  from the environment to the brownian particle. We assume the first and second moments  $\langle \delta p \rangle = 0$  and  $\langle \delta p^2 \rangle = \sigma^2$ . When  $N$  is large the central limit theorem states that the random variable  $\Delta P$  has a gaussian distribution with  $\langle P \rangle = 0$  and  $\langle \Delta P^2 \rangle = N\sigma^2$ . If we consider the momentum change  $\Delta P$  over a discrete time  $\Delta t$ , where the number of collisions is proportional to time  $N \propto \Delta t$ , the corresponding fluctuation force  $R = \Delta P / \Delta t$  will have a variance

$$\langle R^2 \rangle = \frac{\langle \Delta P^2 \rangle}{\Delta t^2} = \frac{N\sigma^2}{\Delta t^2} \propto \frac{1}{\Delta t}.$$

In a computer simulation we need to pick a random force  $R(t)$  from a Gaussian distribution every time-step  $\Delta t$ . These forces will not be correlated as long as  $\Delta t$  is larger than the correlation time of the forces from the molecules which we will assume for this model (I think there exist corrections for this to refer to here). With this assumption we can write the correlation function as

$$\langle R(t)R(0) \rangle = \begin{cases} \frac{a}{\Delta t}, & |\Delta t| < \Delta t/2 \\ 0, & |\Delta t| > \Delta t/2, \end{cases} \quad (1.15)$$

where  $a$  is some strength of (...?). In the limit  $\Delta t \rightarrow 0$  the correlation function becomes

$$\langle R(t)R(0) \rangle = a\delta(t), \quad (1.16)$$

where  $\delta$  denotes the dirac delta function. This is valid for all spatial coordinates which will all be independent of each other. Since both the drag force and the fluctuation force originate from the molecular fluid, where the drag force  $-\alpha v$  is velocity dependent it is reasonable to assume that fluctuation force is independent of velocity, i.e.  $\langle R_i v_j \rangle = 0$  for all cartesian indices  $i$  and  $j$ .

In the following we will attempt justify the Langevin equation (why it is like it is) and determine the relationship between the drag coefficient  $\gamma$  and the random force  $R$ .

From the Langevin equation eq. (1.14) we can compute the velocity autocorrelation function (Move to appendix?). We do this in one dimension for simplicity. We begin by multiplying by  $(e^{\gamma t/m})/m$

$$\dot{v}(t)e^{\gamma t/m} + \frac{\gamma}{m}v(t)e^{\gamma t/m} = \frac{F}{m}e^{\gamma t/m},$$

and integrate from  $t = -\infty$ . By the use of integration by parts on the latter term on the left hand side we calculate the velocity

$$\begin{aligned} \int_{-\infty}^t dt' \dot{v}(t')e^{\gamma t'} + \frac{\gamma}{m}v(t)e^{\gamma t'} &= \int_{-\infty}^t dt' e^{\gamma t'} \frac{F(t')}{m} \\ \int_{-\infty}^t dt' \dot{v}(t')e^{\gamma t'} + \left( \left[ v(t')e^{\gamma t'} \right]_{-\infty}^t - \int_{-\infty}^t dt' \dot{v}(t')e^{\gamma t'} \right) &= \int_{-\infty}^t dt' e^{\gamma t'} \frac{F(t')}{m} \\ v(t) &= \int_{-\infty}^t dt' e^{\frac{-\gamma(t-t')}{m}} \frac{F(t')}{m}, \end{aligned}$$

where  $e^{\frac{-\gamma t}{m}}$  plays the role of a response function. We can then calculate the autocorrelation

$$\begin{aligned} \langle v(t)v(0) \rangle &= \int_{-\infty}^t dt_1 \int_{-\infty}^0 dt_2 e^{\frac{t-t_1-t_2}{m}} \frac{\langle F(t_1)F(t_2) \rangle}{m^2} \\ &= \int_{-\infty}^t dt_1 \int_{-\infty}^0 dt_2 e^{\frac{t-t_1-t_2}{m}} \frac{a\delta(t_1-t_2)}{m^2} \\ &= \int_{-\infty}^0 dt_2 e^{\frac{t-2t_2}{m}} \frac{a}{m^2} = \frac{a}{2m\gamma} e^{-\frac{\gamma t}{m}}, \end{aligned}$$

where we used eq. (1.16) and the fact that the integration commutes with the average (we are allowed to flip the order). By comparing this with the equipartition theorem we get

$$\begin{aligned}\frac{1}{2}m\langle v^2 \rangle &= \frac{k_B T}{2} \\ \frac{1}{2}m\langle v(0)v(0) \rangle &= \frac{a}{4\gamma} = \frac{k_B T}{2} \\ a &= 2\gamma k_B T\end{aligned}$$

We notice the appearance of  $\gamma$  meaning that the magnitude of the fluctuations increase both with friction and temperature. Further we can integrate the velocity over time to get displacement  $x(t)$  and show that the variance (show this? In appendix maybe?) is

$$\langle x^2(t) \rangle = \frac{2k_B T}{\gamma} \left( t - \frac{m}{\gamma} \left( 1 - e^{-\gamma t/m} \right) \right),$$

where for  $t \gg m/\gamma$  only the  $t$ -term survives yielding

$$\langle x^2(t) \rangle = 2k_B T t / \gamma.$$

In 1D, the diffusion constant  $D$  is related to the variance as  $\langle x^2 \rangle = 2Dt$ , meaning that this represents the einstein relation  $D = \mu k_B T$  with the mobility  $\mu = 1/\gamma$ .

when  $t \ll m/\gamma$  we use the Taylor expansion  $1 - e^{-x} \approx x - x^2/2$  for  $x \ll 1$  to get

$$\langle x^2(t) \rangle = \frac{k_B T}{m} t^2$$

which exactly matches the thermal velocity

$$v_{\text{th}} \frac{\langle x^2(t) \rangle}{t^2} = \frac{k_B T}{m}$$

which follows from the equipartition theorem. The finite correlation time  $\gamma/m$  hence describe the crossover from the ballistic regime  $\sqrt{\langle x^2(t) \rangle} \propto t$  to the diffusive regime  $\sqrt{\langle x^2(t) \rangle} \propto \sqrt{t}$ .

Introduce the fluctuation-dissipation theorem concept earlier since this is a motivation for the Langevin equation.

### 1.2.3.2 Implementing Langevin

The implementation of the Langevin equation into LAMMPS follows [33] and updates the force vector for each particle as

$$\begin{aligned}\mathbf{F} &= \mathbf{F}_c + \mathbf{F}_f + \mathbf{F}_r \\ &= -\nabla U - \gamma m \mathbf{v} + \sqrt{\frac{2k_B T m \gamma}{\Delta t}} \mathbf{h}(t)\end{aligned}\tag{1.17}$$

where  $\mathbf{F}_c$  is the conservative force computed via the usual inter-particle interactions described by the potential  $U$ ,  $\mathbf{F}_f$  is the drag force and  $\mathbf{F}_r$  is the random fluctuation force where  $\mathbf{h}$  is a random vector drawn from a normal distribution with zero mean and unit variance. Notice that this generalized description of the Langevin equation deviates from the presentation in eq. (1.14) since we have added the conservative force  $\mathbf{F}_c$ , but also by the appearance of the mass in both the drag force and the fluctuation force due to the introduction of damping. It is beyond our scope to comprehend this. However, the fact that  $\Delta t$  now appears in the denominator for the random force variance  $2k_B T m \gamma / \Delta t$  is due to the fact that we have discretized time. This is in agreement with the formulation in eq. (1.15). By applying eq. (1.17) we get the refined velocity verlet scheme

$$\begin{aligned}\mathbf{v}_i(t + \Delta t/2) &= \mathbf{v}_i(t) - \frac{\Delta t}{2} \left( \frac{\nabla_i U(t)}{m_i} + \gamma \mathbf{v}_i \right) + \sqrt{\frac{k_B T \gamma \Delta t}{2m_i}} \mathbf{h}_i \\ \mathbf{r}_i(t + \Delta t) &= \mathbf{r}_i(t) + \mathbf{v}_i(t + \Delta t/2) \Delta t \\ \mathbf{v}_i(t + \Delta t) &= \mathbf{v}_i(t + \Delta t/2) - \frac{\Delta t}{2} \left( \frac{\nabla_i U(t + \Delta t)}{m_i} + \gamma \mathbf{v}_i(t + \Delta t/2) \right) + \sqrt{\frac{k_B T \gamma \Delta t}{2m_i}} \mathbf{h}_i\end{aligned}$$

with new random vector  $\mathbf{h}_i$  for each particle and each update. Notice however, that LAMMPS only apply this scheme to the particle groups with the thermostat on.

#### 1.2.4 MD limitations (?)

#### 1.2.5 LAMMPS

### 1.3 Defining the system

#### 1.3.1 Region definitions (Sheet, pullblocks and substrate)

Include figure of system to point out thermo layers and freeze layers.

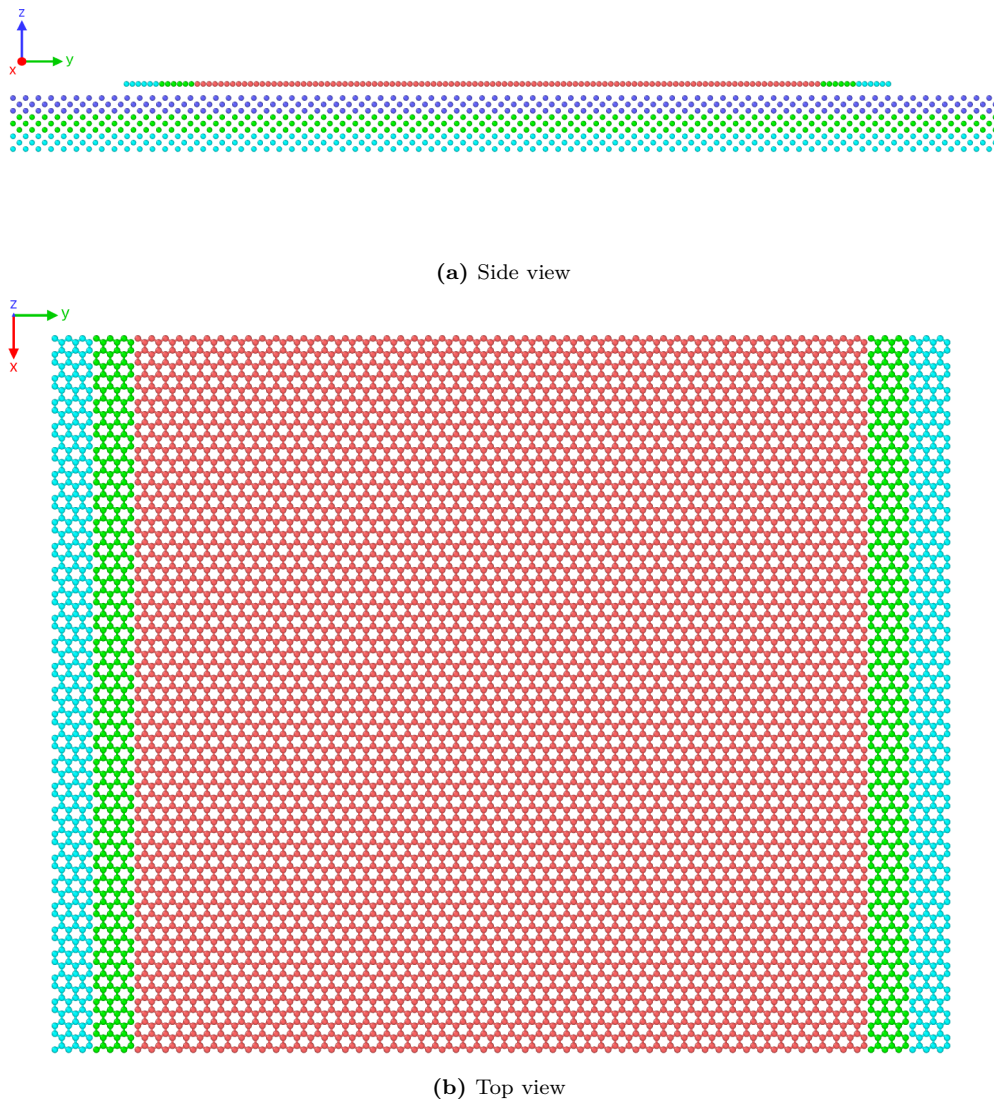


**Figure 1.8:** System. 27456 atoms in total: 7272 with thermostat (orange), 7272 is locked (light blue) and the remaining 12912 just with NVE. (Get better colors)

**Table 1.5:** System atom count and region division.

Region	Total	Sub region	Sub total	NVE	NVT	Locked
Sheet	7800	Inner sheet	6360	6360	0	0
		Pull blocks	1440	0	720	720
Substrate	19656	Upper	6552	6552	0	0
		Middle	6552	0	6552	0
		Bottom	6552	0	0	6552
All	27456			12912	7272	7272

The sheet dimensions are

**Table 1.6:** Sheet dimensions

Group	$x, y$ -dim	dim [Å]	Area [Å <sup>2</sup> ]
Full sheet	$x_S \times y_S$	$130.029 \times 163.219$ Å	21,223.203
Inner sheet	$x_S \times 81.40\%_{y_s}$	$130.029 \times 132.853$ Å	17,274.743
Pull blocks	$2 \times x_S \times 9.30\%_{y_s}$	$2 \times 130.029 \times 15.183$ Å	$2 \times 1,974.230$

### 1.3.2 Numerical procedure

1. Relax (15 ps)
2. Stretch
3. Pause 1 (5 ps)
4. Apply normal force (with damper to avoid hard impact)
5. Pause 2 (5 ps)
6. Drag

### 1.3.3 Creating the sheet

We are going to create a 2D sheet graphene sheet.

#### 1.3.3.1 Graphene

Graphene is a single layer of carbon atom, graphite is the bulk, arranged in a hexagonal lattice structure. We can describe the 2D crystal structure in terms of its primitive lattice vector and a basis. That is we populate each lattice site by the given basis and translate it to fill the whole plane by any linear combination of the lattice vectors

$$\mathbf{T}_{mn} = m\mathbf{a}_1 + n\mathbf{a}_2, \quad m, n \in \mathbb{N}.$$

For graphene we have the primitive lattice vectors

$$\mathbf{a}_1 = a \left( \frac{\sqrt{3}}{2}, -\frac{1}{2} \right), \quad \mathbf{a}_2 = a \left( \frac{\sqrt{3}}{2}, \frac{1}{2} \right), \quad |\mathbf{a}_1| = |\mathbf{a}_2| = 2.46 \text{ Å}.$$

Notice that we deliberately excluded the third coordinate as we only consider a single graphene layer on not the bulk graphite consisting of multiple layers stacked on top of each other. The basis is

$$\left\{ (0,0), \frac{a}{2} \left( \frac{1}{\sqrt{3}}, 1 \right) \right\}$$

It turns out that the spacing between atoms is equal for all pairs with an interatomic distance

$$\left| \frac{a}{2} \left( \frac{1}{\sqrt{3}}, 1 \right) \right| \approx 1.42 \text{ Å}.$$

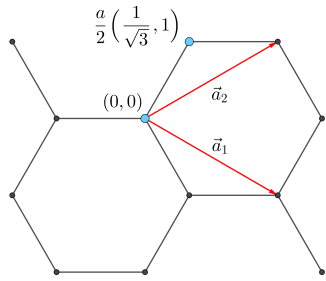


**Figure 1.9:** Graphene crystal structure with basis.

### 1.3.3.2 Indexing

In order to define the cut patterns applied to the graphene sheet we must define an indexing system. We must ensure that this gives an unique description of the atoms as we eventually want to pass a binary matrix, containing 0 for removed atom and 1 for present atom, that uniquely describes the sheet. We do this by letting the x-coordinate point to zigzag chains and the y-coordinate to the position along that chain. This is illustrated in figure 1.10. Other solutions might naturally invoke the lattice vectors, but as these only can be used to translate to similar basis atoms a unfortunate duality is introduced as ones need to include the basis atom of choice into the indexing system. With the current system we notice that locality is somewhat preserved. That is, atom  $(i, j)$  is in the proximity of  $\{(i + 1, j), (i - 1, j), (i, j + 1), (i, j - 1)\}$ , but only three of them is categorized as nearest neighbours due to the hexagonal structure of the lattice. While  $(i, j \pm 1)$  is always nearest neighbours the neighbour in the x-direction flip sides with incrementing y-coordinate. That is the nearest neighbours (NN) is decided as

$$\begin{aligned} j \text{ is even} &\rightarrow \text{NN} = \{(i + 1, j), (i, j + 1), (i, j - 1)\}, \\ j \text{ is odd} &\rightarrow \text{NN} = \{(i - 1, j), (i, j + 1), (i, j - 1)\}. \end{aligned}$$

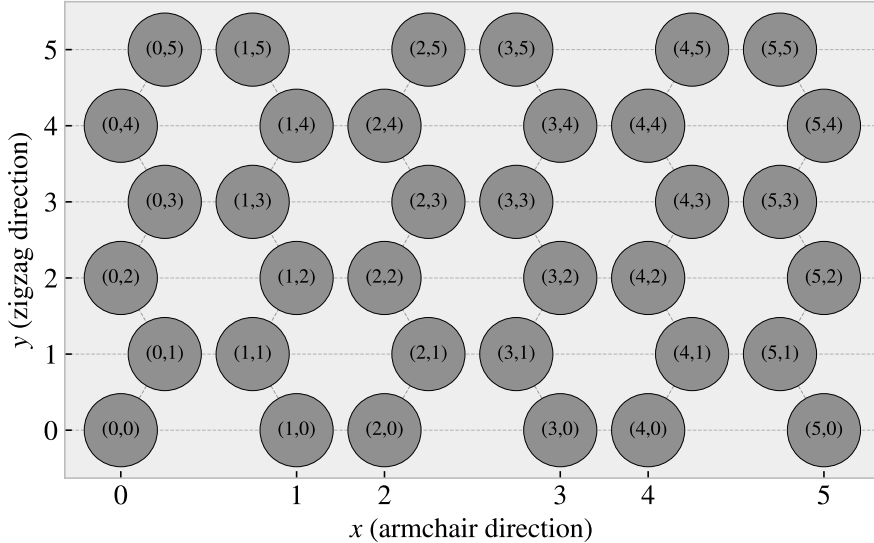


**Figure 1.10:** Graphene atom indexing

### 1.3.3.3 Removing atoms

As a mean to ease the formulation of cut patterns we introduce pseudo center element in each gap of the hexagonal honeycombs, see figure 1.11.

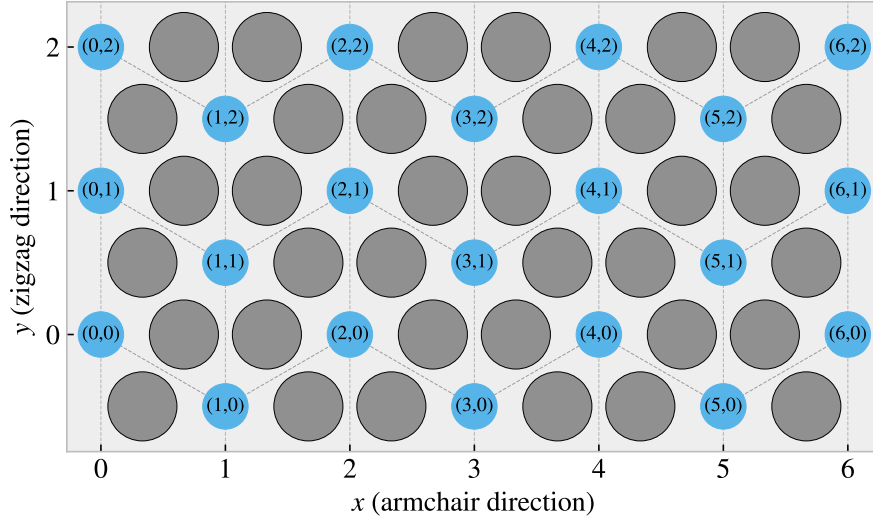


Figure 1.11: Graphene center indexing

Similar to the case of the indexing for the carbon atoms themselves the nearest neighbour center elements alternate with position, this time along the x-coordinate. Each center element has six nearest neighbours, in clock wise direction we can denote them: “up”, “upper right”, “lower right”, “down”, “lower left”, “upper left”. The “up” and “down” is always accessed as  $(i, j \pm 1)$ , but for even  $i$  the  $(i + 1, j)$  index corresponds to the “lower right” neighbour while for odd  $i$  this corresponds to the “upper right” neighbour. This shifting applies for all left or right neighbours and the full neighbour list is illustrated in figure 1.12.

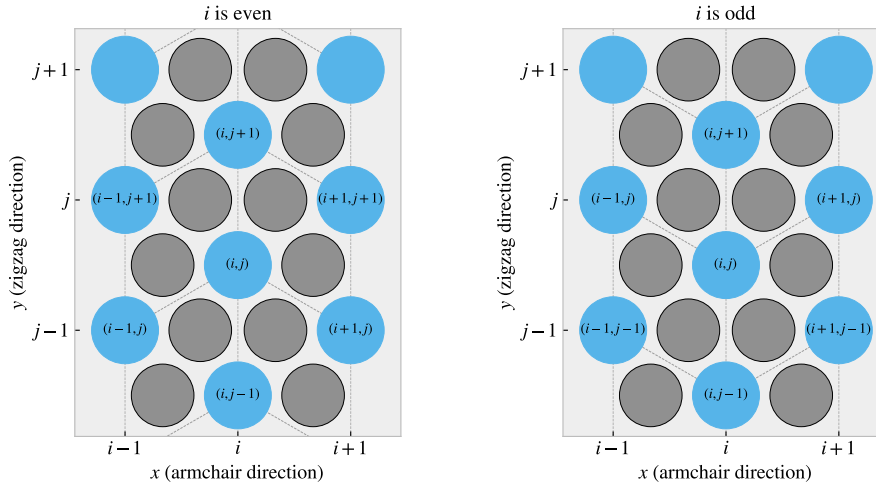


Figure 1.12: Graphene center elements directions

We define a cut pattern by connecting center elements into connected paths. As we walk element to element we remove atoms according to one of two rules

1. Remove intersection atoms: We remove the pair of atoms placed directly in the path we are walking. That is, when jumping to the “up” center element we remove the two upper atoms located in the local hexagon of atoms. This method is sensitive to the order of the center elements in the path.

2. Remove all surrounding atoms: We simply remove all atoms in the local hexagon surrounding each center element. This method is independent of the ordering of center elements in the path.

We notice that removing atoms using either of these rules will not guarantee an unique cut pattern. Rule 1 is the more sensitive to paths but we realize that, for an even  $i$ , we will remove the same five atoms following either of the following paths.

$$(i, j) \rightarrow \underbrace{(i+1, j+1)}_{\text{upper right}} \rightarrow \underbrace{(i, j+1)}_{\text{up}} \rightarrow \underbrace{(i+1, j+2)}_{\text{upperright + up}} \rightarrow \underbrace{(i+1, j+1)}_{\text{upper right}}$$

$$(i, j) \rightarrow \underbrace{(i+1, j+1)}_{\text{upper right}} \rightarrow \underbrace{(i+1, j+2)}_{\text{upperright + up}} \rightarrow \underbrace{(i, j+1)}_{\text{up}}$$

For rule 2 it is even more obvious that different paths can result in the same atoms being removed. This is the reason that we needed to define and indexing system for the atom position itself even though that all cuts generated manually will use the center element path as reference.

Illustrate some delete path?

### 1.3.4 Kirigami patterns

#### 1.3.4.1 Pop-up

#### 1.3.4.2 Honeycomb

#### 1.3.4.3 Random walk

## 1.4 Pressure reference

Find place to put this.

In order to relate the magnitude of the normal force in our friciton measurement we will use the pressure as a reference. We will use the pressure underneath a stiletto shoe as a worst case for human pressure execution underneath the shoes. From (source 1) it is reported that the diameter of a stiletto heeled shoe can be less than 1 cm. Hence a 80 kg man<sup>3</sup> standing on one stiletto heels (with all the weight on the heel) will result in a pressure corresponding diameter of

$$P = \frac{F}{A} = \frac{mg}{r^2\pi} = \frac{80 \text{ kg} \cdot 9.8 \frac{\text{m}}{\text{s}^2}}{(\frac{1 \times 10^{-2} \text{ m}}{2})^2\pi} = 9.98 \text{ MPa}$$

While this is in itself a spectacular realization that is often used in introduction physics courses (source 2) to demonstrate the rather extreme pressure under a stiletto heel (greater than the foot of an elephant) (how many Atmos) this serves as a reasonable upperbound for human executed pressure. With a full sheet area of  $\sim 21 \times 10^3 \text{ \AA}^2$  we can achieve a similar pressure of  $\sim 10 \text{ MPa}$  with a normal force

$$F_N = 10 \text{ MPa} \cdot 21 \times 10^{-17} \text{ m}^2 = 2.10 \text{ nN}$$

Of course this pressure might be insufficient for various industrial purposes, but with no specific procedure in mind this serves as a decent reference point. Notice that if we consider a human foot with area  $113 \text{ cm}^2$  the pressure drops to a mere 70 kPa corresponding to  $\sim 0.01 \text{ nN}$ .

## 1.5 Fourier Transform (light)

Find out where to put this if necessary.

---

<sup>3</sup>Yes, a man can certainly wear stiletto heals.

Fourier transform is a technique where we transform a function  $f(t)$  of time to a function  $F(k)$  of frequency. The Forward Fourier Transform is done as

$$F(k) = \int_{-\infty}^{\infty} f(t)e^{-2\pi i k x} dx$$

For any complex function  $F(k)$  we can decompose it into magnitude  $A(k)$  and phase  $\phi(k)$

$$F(k) = A(k)e^{i\phi(k)}$$

Hence when performing a Forward Fourier transform on a time series we can determine the amplitude and phase as a function of frequency as

$$A(k) = |F(k)|^2, \quad \phi(k) = \Im \ln F(k)$$

- Real life procedures to mimic in computation, for instance Atomic Force Microscopy (AFM) for friction measurements.
- Available technology for test of my findings if successful (possibilities for making the nano machine)

## 1.6 Machine Learning (ML)

- Feed forward fully connected
- CNN
- GAN (encoder + decoder)
- Genetic algorithm
- Using machine learning for inverse designs partly eliminate the black box problem. When a design is produced we can test it, and if it works we not rely on machine learning connections to verify it's relevance.
- However, using explanations techniques such as maybe t-SNE, Deep dream, LRP, Shapley values and linearizations, we can try to understand why the AI chose as it did. This can lead to an increased understanding of each design feature. Again this is not dependent on the complex network of the network as this can be tested and verified independently of the network.

### 1.6.1 Feed forward network / Neural networks

### 1.6.2 CNN for image recognition

### 1.6.3 GAN (encoder + decoder)

### 1.6.4 Inverse design using machine learning

### 1.6.5 Prediction explanation

#### 1.6.5.1 Shapley

#### 1.6.5.2 Linearizations

#### 1.6.5.3 LRP

#### 1.6.5.4 t-SNE

# Simulations

## 1.7 Baseline study

Consider relabeling drag length to sliding distance instead.

### 1.7.1 Variable overview

The friction measurement simulation is governed by the following parameters, which is divided into three sub categories for the purpose of this thesis as shown in table 1.7.

**Table 1.7:** Parameters of the numerical procedure for measuring friction.

Category	Parameter name: description	Category purpose
Physical	<ul style="list-style-type: none"> <li>- <math>T</math>: Temperature for the Langevin thermostat.</li> <li>- <math>v_{drag}</math>: Drag speed for the sheet translation.</li> </ul>	Parameters that we expect to have an inevitably effect on the system friction properties, for which the choice will be a baseline for our studies.
Measurement	<ul style="list-style-type: none"> <li>- <math>dt</math>: Integration timestep.</li> <li>- <math>t_R</math>: Relaxtion time before strething.</li> <li>- Pauses between stretch and adding normal force and between dragging the sheet.</li> <li>- Stretch Speed: How fast to stretch the sheet.</li> <li>- <math>K</math>: Spring constant for the spring responsible of translating the sheet. An infinite spring constant is achieved by moving the end blocks as a rigid body (Lammps: fix move).</li> <li>- Drag Length: How far to translate the sheet.</li> <li>- Sheet size: Spatial size of the 2D sheet.</li> </ul>	Paramters that effects the simulation dynamics and the 'experimental procedure' that we are mimicking. We aim to choose these paramters such that the friction properties is stable for small perturbations.
ML input	<ul style="list-style-type: none"> <li>- Sheet configuration: A binary matrix containing information of which atoms is removed (0) and which is still present (1) in the graphene structure.</li> <li>- Scan angle: The direction for which we translate the sheet.</li> <li>- Stretch amount: The relative sheet stretch in percentage.</li> <li>- <math>F_N</math>: Applied normal force to the end blocks.</li> </ul>	The ramaining paramters that serve as the governing variables in the optimization process for certain friction properties and is thus the input variables for the ML part.

We should try to set the phycis and measurement parameters in such a way that we reduce computation speed where it is doesn't infer with the frictional properties study.

We need to define some ranges for the ML input paramters.  $F_N$ , stretch ranges where it is not prone to ruptures. The configuration it self does not have clear rules but is also being regulated by the no rupture requirement.

## 1.7.2 Raw data analysis

### 1.7.2.1 Force oscillations

We first assess the raw data for the friction force  $F_{\parallel}$  parallel to the drag direction as seen in figure 1.13. The sample rate is  $10 \text{ ps}^{-1}$  for which we sample the mean of all previous timesteps. We observe that the data carriers oscillations on different time scales. By applying a savgol filter to data with a polyorder of 5 and window length corresponding to a drag length of  $3.0 \text{ \AA}$  (or time interval  $15.0 \text{ ps}$ ) we can qualitatively point out at least two different frequencies of oscillation. On figure 1.13a we see roughly three waves on the savgol filter corresponding to one frequency, while on 1.13b the same savgol filter reveals an even slower frequency on top of the first creating a visual patterns of a wavepacket.

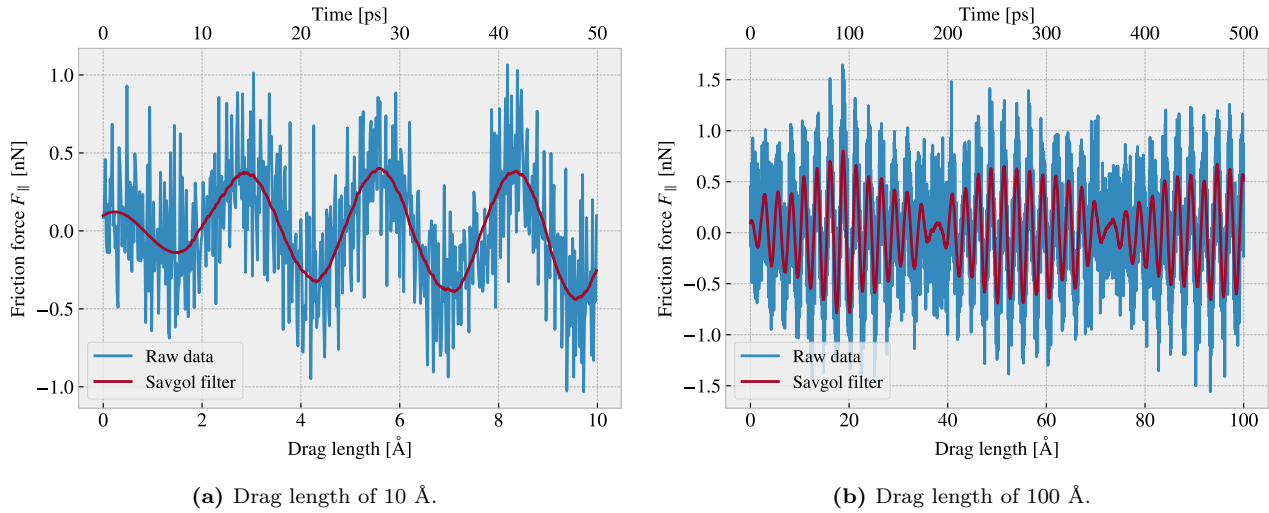


**Figure 1.13:** Friction force  $F_{\parallel}$  between (full) sheet and substrate with respect to the drag direction vs. drag length. The drag length is measured by the constant movement of the virtual atom and not the COM of the sheet. The red line represents a savgol filter with window polyorder 5 and window length 150 (corresponding to a drag length of  $3 \text{ \AA}$  or a time window of  $15 \text{ ps}$ )

By performing a Forward Fourier Transform of the data (using FFT) we can quantitatively identify some of the leading frequencies as seen in figure 1.14a. By plotting the two most dominant frequencies  $f_1 = 0.0074 \text{ ps}^{-1}$  and  $f_2 = 0.0079 \text{ ps}^{-1}$  as  $\sin(2\pi f_1) + \sin(2\pi f_2)$  we find a convincing fit to the observed wavepacket shape as seen in figure 1.14b. By using the trigonometric identity

$$\begin{aligned}\sin(\alpha + \beta) &= \sin(\alpha)\cos(\beta) + \cos(\alpha)\sin(\beta), \\ \sin(\alpha - \beta) &= \sin(\alpha)\cos(\beta) - \cos(\alpha)\sin(\beta),\end{aligned}$$

and decomposing  $f_1 = a - b$ ,  $f_2 = a + b$  we can rewrite the sine sum as the sinusoidal product

$$\begin{aligned}\sin(2\pi f_1)\sin(2\pi f_2) &= \sin(2\pi(a - b))\sin(2\pi(a + b)) \\ &= \sin(a)\cos(b) + \cancel{\cos(2\pi a)\sin(2\pi b)} + \sin(2\pi a)\cos(2\pi b) - \cancel{\cos(2\pi a)\sin(2\pi b)} \\ &= 2\sin(2\pi a)\cos(2\pi b),\end{aligned}$$

with

$$\begin{aligned}a &= \frac{f_1 + f_2}{2} = 0.0763 \pm 0.0005 \text{ ps}^{-1}, & b &= \frac{f_2 - f_1}{2} = 0.0028 \pm 0.0005 \text{ ps}^{-1}, \\ &= 0.381 \pm 0.003 \text{ \AA}^{-1}, & &= 0.014 \pm 0.003 \text{ \AA}^{-1},\end{aligned}$$

where the latter frequency is denoted with respect to drag length. This makes us recognize the fast oscillation frequency as  $a$  and the slower frequency as  $b$ . The faster one has a period of  $T_a = 1/a = 2.62 \pm 0.02 \text{ \AA}^4$ . This

<sup>4</sup>The uncertainty  $\Delta y$  is calculated as  $\Delta y = \left| \frac{\partial y}{\partial x} \Delta x \right|$  for uncertainty  $\Delta x$  and  $y(x)$

corresponds well with the magnitude of the lattice spacing and especially that of graphene  $a = 2.46 \text{ \AA}$  (as predicted theoretically: make reference to self or other). We also take note of the longest period in the data  $T_b = 71 \pm 15 \text{ \AA}^{-1}$  which will be relevant for the evaluation of measurement uncertainty.

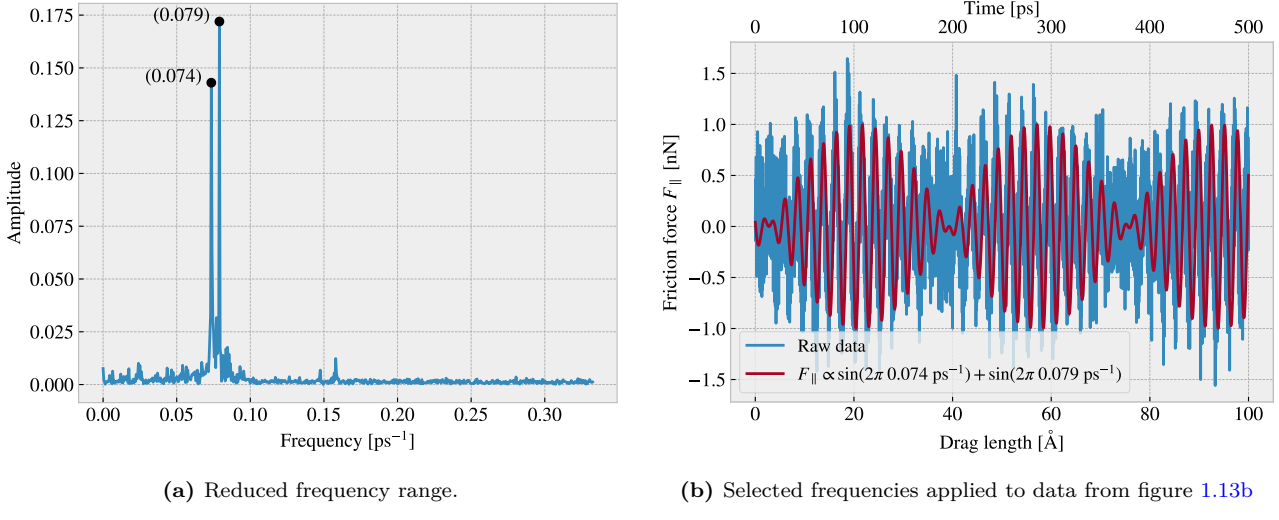


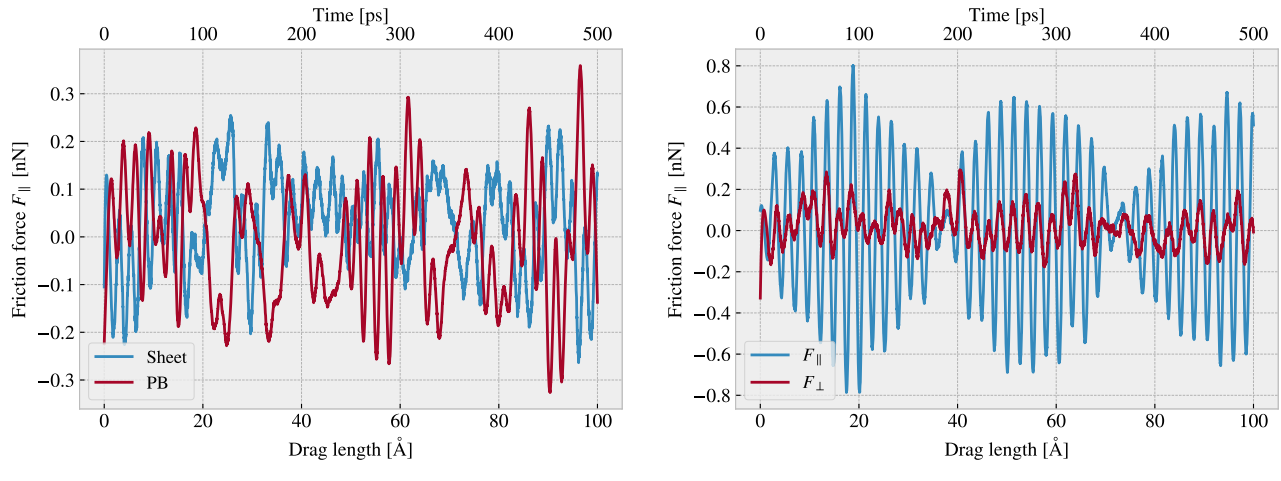
**Figure 1.14:** Fourier transform on data shown in figure 1.13b.

### 1.7.2.2 Decompositions

In the previous analysis we have looked only at the friction force for the full sheet, including the pullblocks which is locked off during the drag, and with respect to the drag direction.

Since we are only applying cuts to the inner sheet (excluding the pull blocks), it might seem more natural to only consider the friction on that part. If the desired frictional properties can be observed from the inner sheet we can always scale the relative size between inner sheet and pull block. However, when looking at the time series of friction force decomposed onto inner sheet and pull block (figure 1.15a) we observe the friction force arising from those parts is seemingly antisymmetric. That is, the frictional pull on the substrate is oscillating between the inner sheet and the pullblock. Remembering that the normal force is only applied to the pull block we might take this as an integrated feature of the system. An interesting nonlinear friction coefficient might depend on this internal distribution of forces. Hence, we hedge our bets and use the full sheet friction force as holistic approach to the measurement problem.

Similar we might question the decision of only considering the frictional force projected on the direction of the drag as we are neglecting the “side shift” induced during the drag phase. In figure 1.15b we see the decomposition into force components parallel  $F_{\parallel}$  and perpendicular  $F_{\perp}$  to the drag direction respectively. We see that the most dominant trend is projected into the parallel component. If we want to include the perpendicular component as well we would have to evaluate the friction as the length of the vector for which we lose the sign of direction. Hence we would only get positive contributions, meaning a resisting force, which is not faithfully capturing the sheet oscillations that make the friction forces act both against in with the direction of drag. By this argument we decide to use only the parallel component going forward.



(a) Decomposition into group inner sheet (sheet) and pull blocks (PB). (b) Decomposition into parallel ( $\parallel$ ) and perpendicular ( $\perp$ ) to drag direction.

**Figure 1.15:** Decomposition into parallel ( $\parallel$ ) and perpendicular ( $\perp$ ) to drag direction showing the savgol filter applied

### 1.7.2.3 Center of mass path

From the previous observations we already have evidence of a stick slip behaviour, judging from the friction oscillations in figure 1.13, and motion partial motion perpendicular to the drag direction, judging from the perpendicular force component in figure 1.15b. By looking at the  $x, y$ -position for the center of mass (COM) we can see the stick slip motion manifested as a variation in COM speed combined with a side to side motion as shown in figure 1.16a. To increase this effect we also show the same plot with a spring ... move with spring constant 30 N/m in figure 1.16b. While the max speed is on the same scale the side to side motion is increased (notice that the axis scale is different between figure 1.16a and 1.16a).

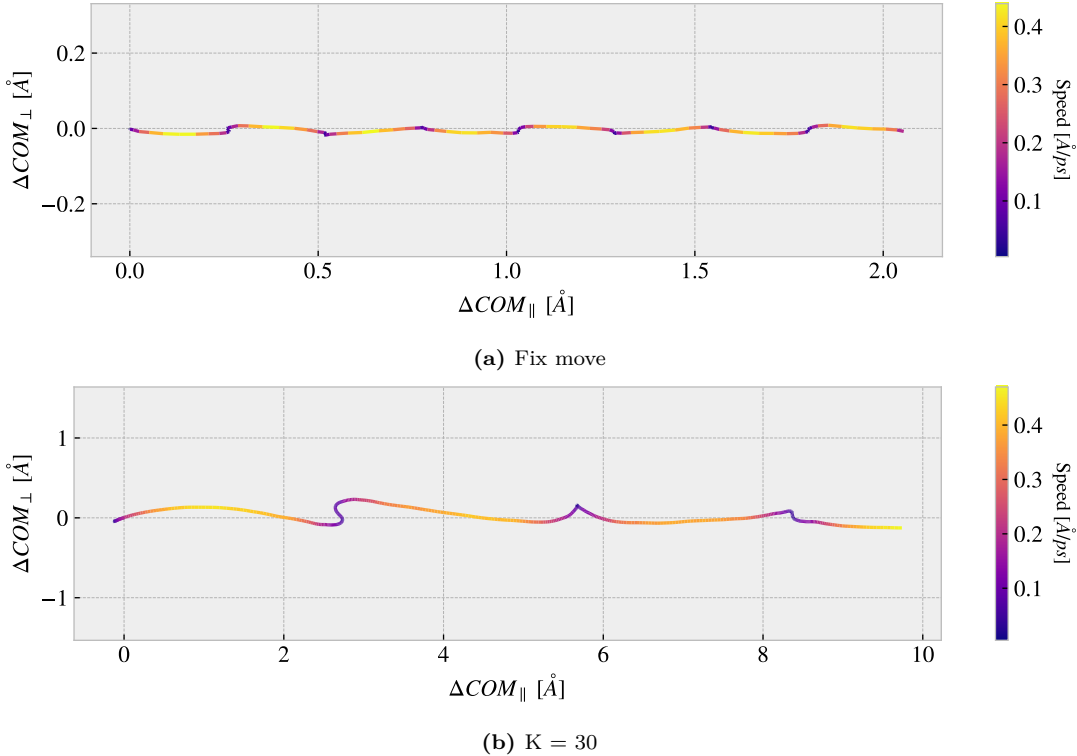


**Figure 1.16:** Center of mass relative position from start of drag phase in terms of axis parallel to drag direction  $\Delta COM_{\parallel}$  and axis perpendicular to drag direction  $\Delta COM_{\perp}$ . The colorbar denotes the absolute speed of the COM.

### 1.7.3 Defining metrics for dynamic and static friction

We are interested taking the comprehensive friction force time series dataset and reducing it into single metrics describing the dynamic and static friction respectively. The natural choice is to use the mean and max values.

#### 1.7.3.1 Dynamic friction

For the dynamic friction measurement we take the mean of the latter half of the data to ensure that the system has stabilized itself before taking the mean. For a full drag simulation of  $400 \text{ \AA}$  we would thus base our mean value on the latter  $200 \text{ \AA}$  drag. In figure 1.17a we have shown the friction force of the first  $10 \text{ \AA}$  of drag together with a running mean with window length 50% of the corresponding data length. The final mean value estimate is indicated with red point at the end and we clearly observe that the length of sampling is insufficient since we get a negative friction force. Nonetheless, one approach to quantify the uncertainty of the final mean estimate is to consider the running mean. The more the running mean fluctuates the more uncertainty is associated with the final estimate.

We should not care for fluctuations in the initial part of the running mean curve as this is still including data from the beginning, where it might transition from static to dynamic friction. Only the running mean “close” to the ending should be considered for our uncertainty. From the Fourier analyse we concluded that longest period of any dominant oscillations is  $\sim 71 \text{ \AA}^{-1}$  corresponding to  $\sim 35\%$  of the running mean window of  $200 \text{ \AA}$  drag. Hence we use standard deviation of the final 35% of the running mean curve to approximate the uncertainty of the final mean value. By dividing with the final running mean we effectively calculate the relative error as shown in figure 1.17b. Naturally, we get a relative error of  $\sim 257\%$  which corresponds with the mean value taking an unexpected negative value.

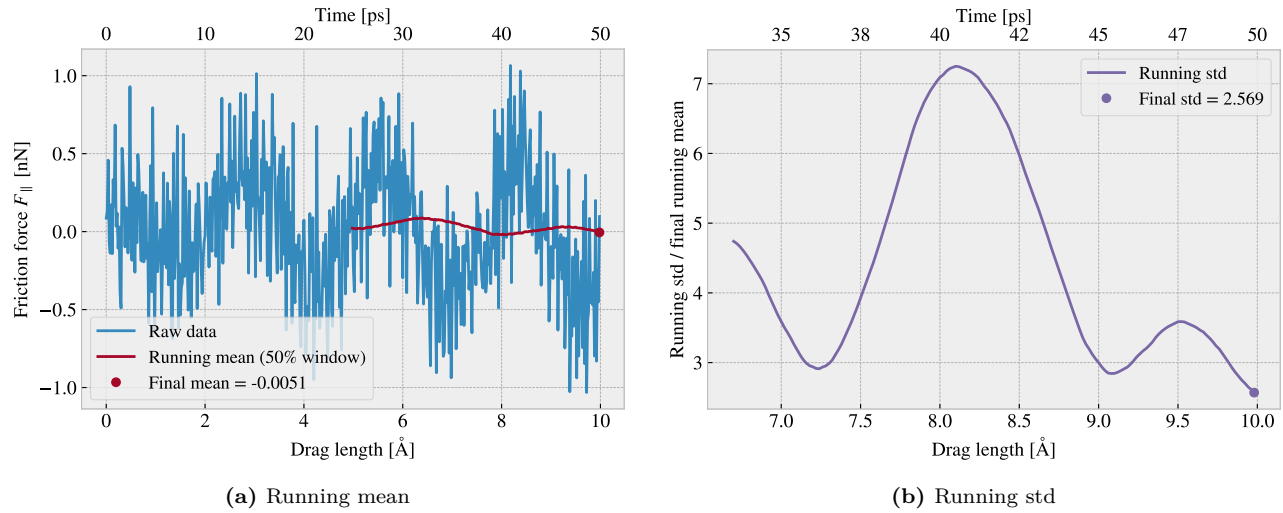


Figure 1.17: Running std

When we include the full 400 Å drag, such that std window actually matches with the longest period of oscillations expected from the data, we get a final relative error of  $\sim 12\%$  as shown in fig 1.18. This is just at the limit for an acceptable error, but as we shall see later (refer to figure or something) this high error is mainly connected to the cases of low friction. When changing the simulation parameters, such that the mean friction evaluate to considerable higher values, the relative error drops to around (put in numbers). One explanation is that the oscillations in the running mean does not increase linearly with the magnitude of the friction, and hence the relative error might spike especially for the low friction cases.

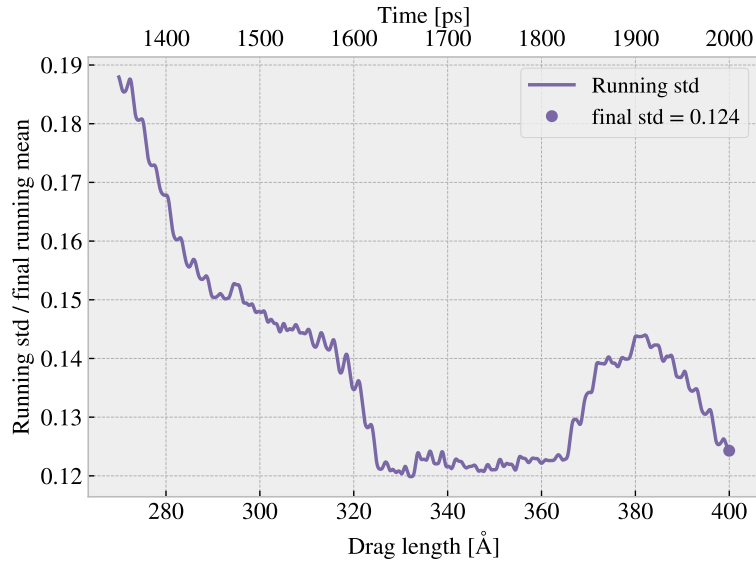


Figure 1.18: ...

### 1.7.3.2 Static friction

The max value is the most obvious choice for addressing the static friction, even though that the definition of the static friction is a bit vague. At least when judging from the raw data in figure 1.13 we not see a textbook example of the static friction precursor (maybe include a classic static friction curve in the theory... I'm not completely sure what to expect here). Additionally the global max value does not always lie in the initial part of the simulation.

For a proper static friction evaluation we should increase force slowly and wait for the slip response. Here we

drag quite fast making it difficult to assess the static response.

We investigate the placement of the max values, i.e. the drag length for which we measure the max friction force. We show the placement of the top three max values for different simulations with varying normal force in figure 1.19. We observe immediately that only a few top three max values are measured within a full slow period of  $\sim 71$  Å. In fact many max values are measured just before the end of the simulation. This indicates that the naive approach of using the overall max value to describe the static friction coefficient might be a too naive approach. Another approach is to use the max value within a single period, but we do not really know if this period will be similar for all cut patterns and thus this might be limiting.

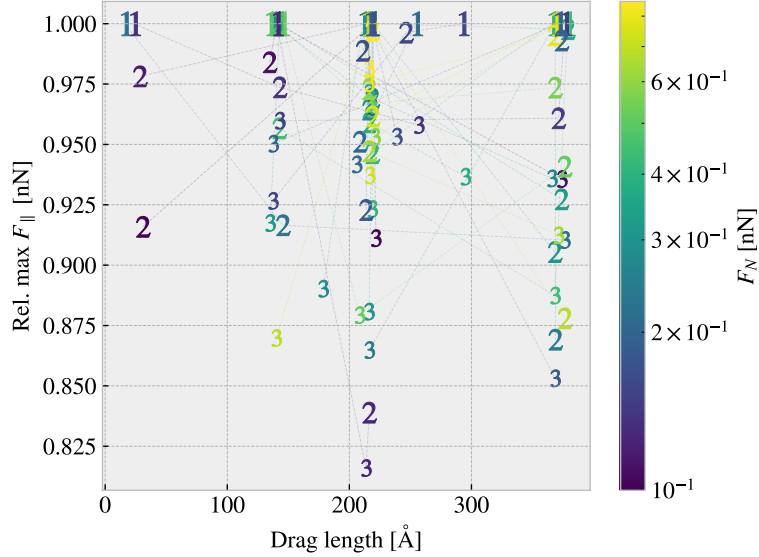


**Figure 1.19:** Distribution of top 3 max values for different normal force

Look into static friction when having a spring connected to the drag force with rather low spring constant. Maybe compare to critical stiffness in FK model. Some rough calculations follow here (make a note about this being a very naive approach to determine a suitable stiffness for static friction scenarios. In reality one should increase force slowly to observe this probably). When dragging the sheet in the y-direction we effectively have a lattice spacing

$$a_c = a_{2,x} + B_x = a_G \frac{\sqrt{3}}{2} + \frac{a_G}{2\sqrt{3}} = \frac{2a_G}{\sqrt{3}}$$

for graphene lattice constant  $a_G = 2.46$  Å. For the diamond silicon structure this is essentially equal to the lattice constant  $a_D = 5.4210$  Å. This gives

$$\theta = \frac{a_c}{a_b} = \frac{2}{\sqrt{3}} \frac{a_G}{a_D} \approx 0.5230.$$

Since we have the factor  $2/\sqrt{3}$  it is safe to assume that this is an irrational number leading to incommensurability. The worst case scenario of incommensurability (where  $\theta$  equals the golden-mean, Can we get the exact number?) gives the minimal critical stiffness  $K_c \sim 2U_0(\frac{\pi}{a_b})^2$ , where  $U_0$  is the substrate potential magnitude and  $a_b$  the lattice spacing of the substrate. The potential barrier  $U_0$  can be approximated by the work done when resisting the normal force as  $\sim F_N a_D/2$  such that the critical stiffness can be approximated to

$$K_c \sim 2F_N \frac{a_D}{2} \left( \frac{\pi}{a_D} \right)^2 = \frac{F_N}{a_D} \pi^2$$

With a normal force of 1 nN we get  $K_c \sim 18$  N/m. Hence, we should try a spring constant lower than that as a qualified way of determining if this is the reason why we do not really see static friction in the simulation. By

plotting the max position (in terms of drag length) as a function of spring constant as seen in figure 1.20 we can investigate if the concept of a critical spring constant is governing this simulation. However, as I'm writing this I'm realizing that the spring constant in the model applies to the interatomic forces and not the one dragging the system.....

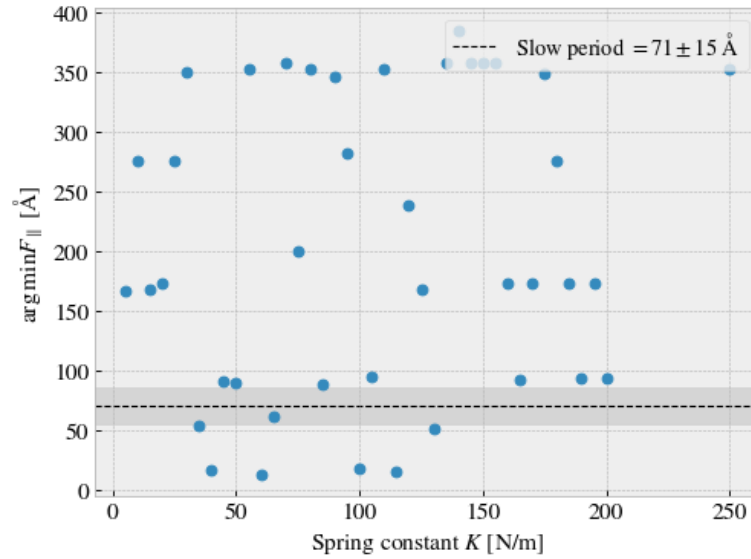


**Figure 1.20:** Displacement for the max peak in friction to appear as a function of spring constant dragging the sheet. Fixmove is tmp mapped to  $K = 200$  here.

### 1.7.4 Investigating selected parameters

Investigate effects of temperature, drag speed, spring constant and dt.

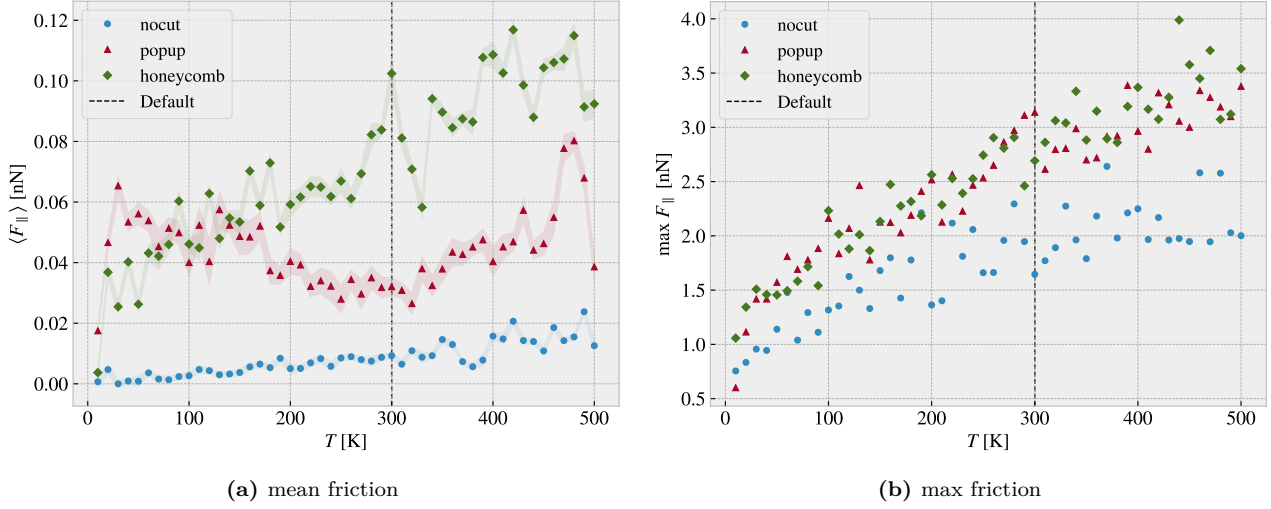


**Figure 1.21:** Temperature.  $v = 20$  m/s and fixmove.

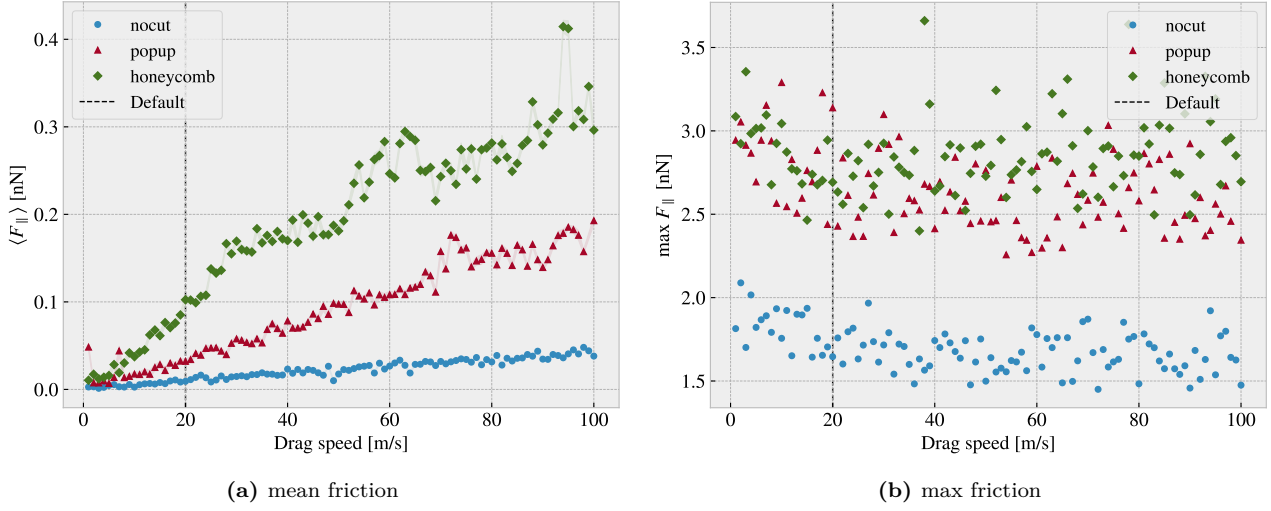


**Figure 1.22:** Drag speed

Simulations of concentric nanotubes in relative motion (telescopic sliding), have revealed the occurrence of well-defined velocities at which friction is enhanced, corresponding to a washboard frequency resonating with longitudinal [172] or circular [173] phonon modes, leading to enhanced energy dissipation. The frictional response becomes highly non-linear while approaching the critical velocity and, contrary to macroscopic systems, washboard resonances can arise at multiple velocities, especially for incommensurate interfaces where more than one length scale may be in common to the contacting surfaces [172] [6].

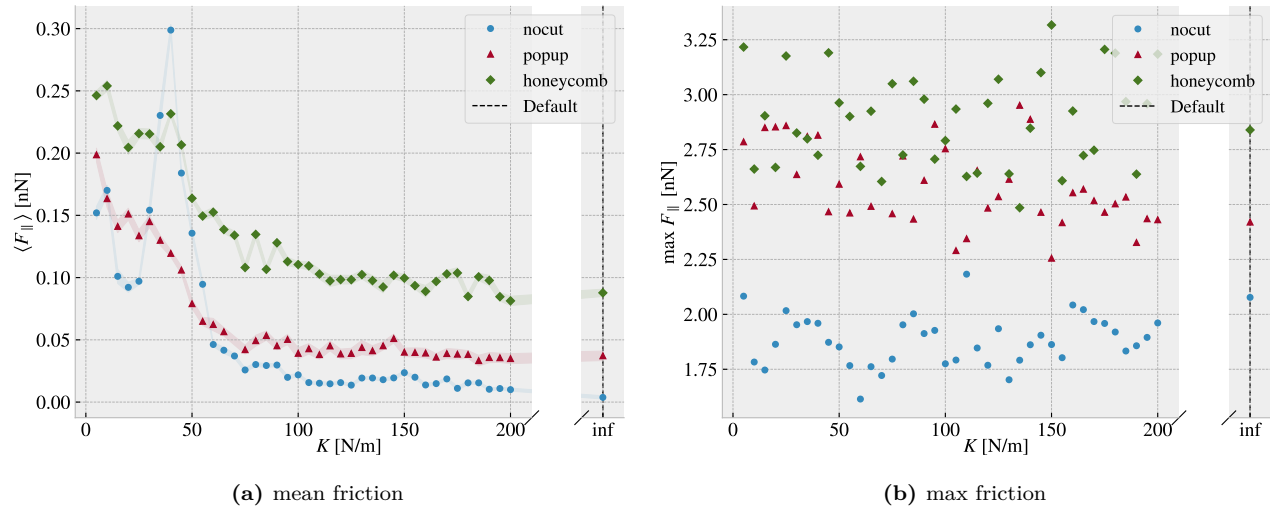


Figure 1.23: Spring constant

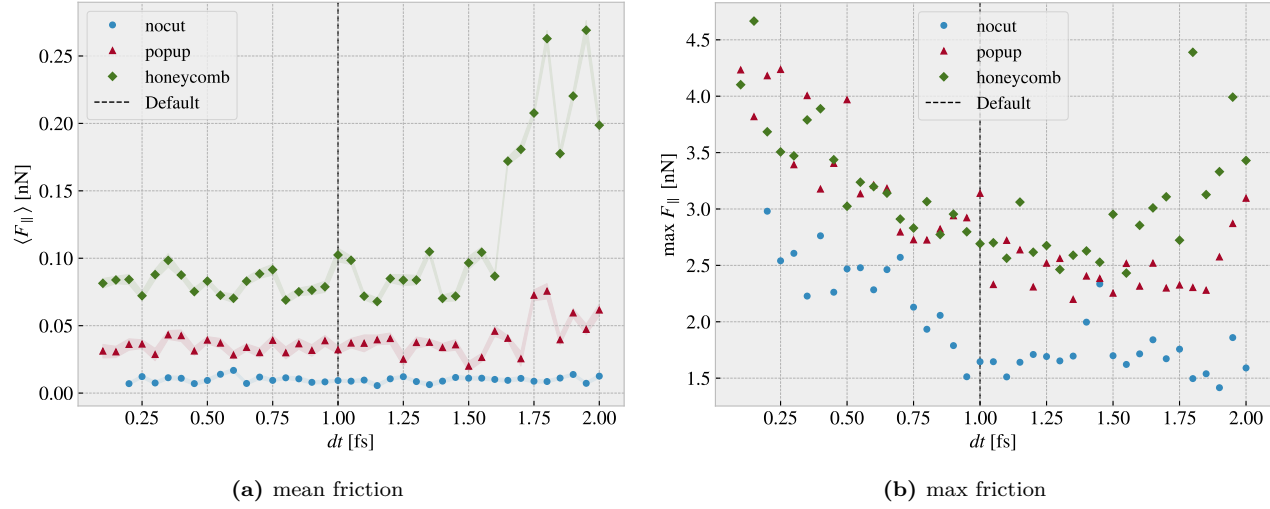


Figure 1.24: Timestep

### 1.7.5 Normal force and stretch dependencies

#### 1.7.5.1 Multi stretch

text

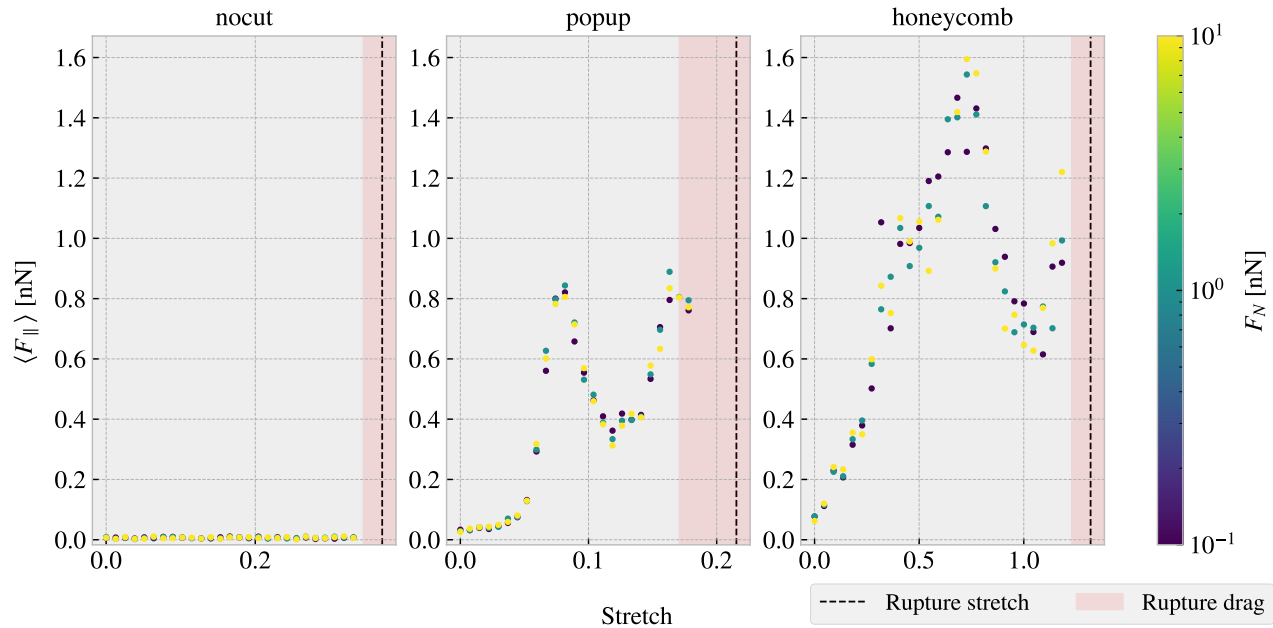


Figure 1.25: ...

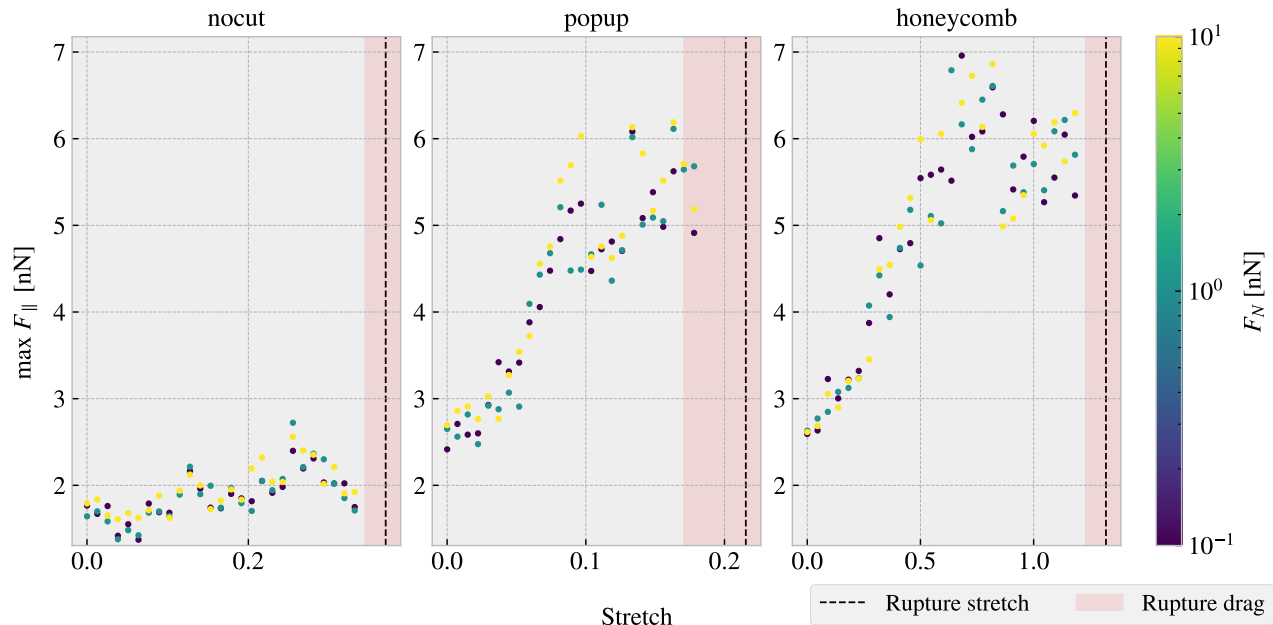


Figure 1.26: ...

### 1.7.5.2 Multi normal force

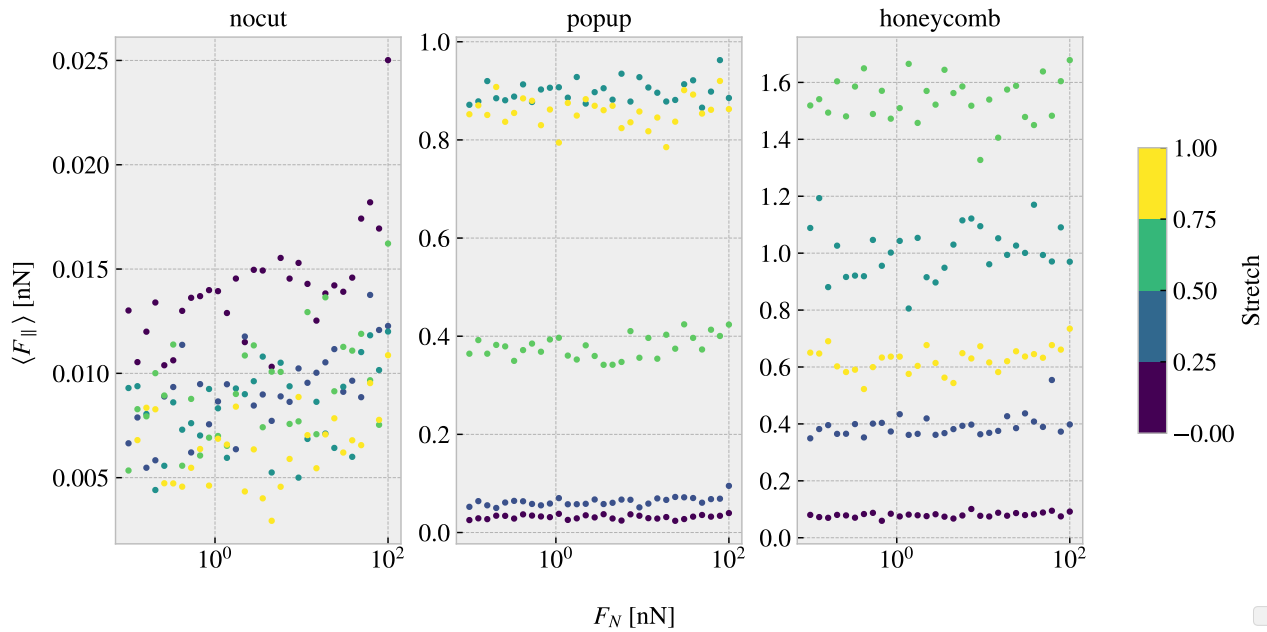


Figure 1.27: ...

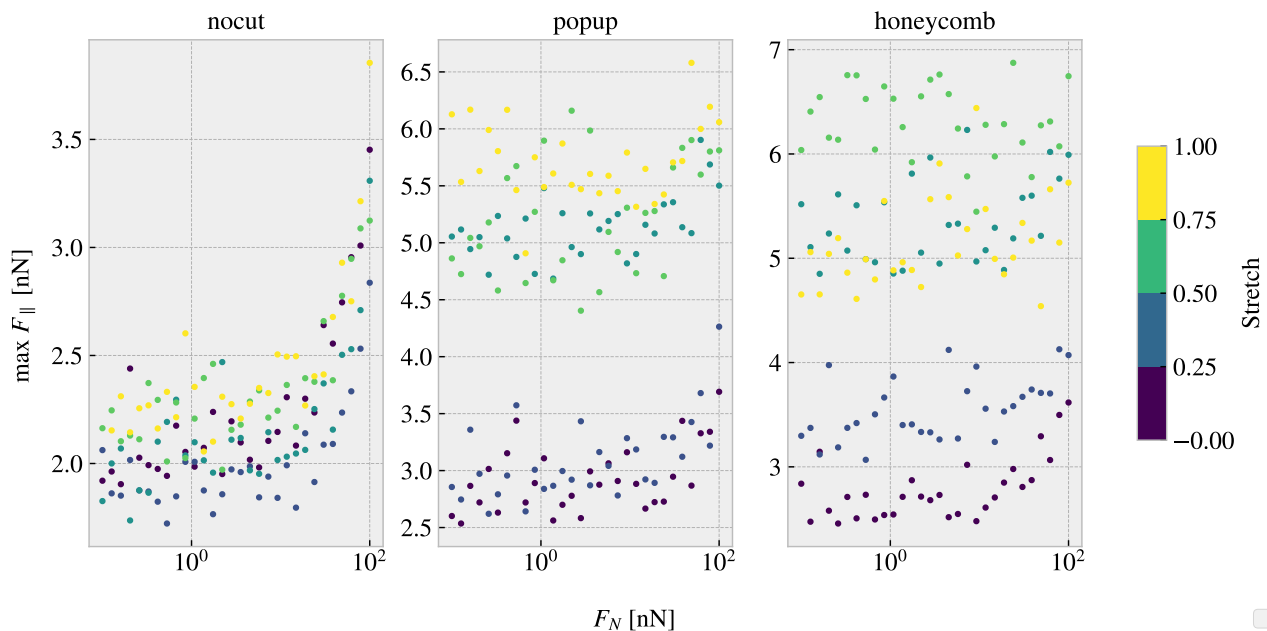


Figure 1.28: Colorbar is only fitted for the right plot (honeycomb)... this should be fixed. Should I have run a linear distribution of FN so I could plot it linear here also...?

**Table 1.8:** Mean friction coeff

nocut	$0.00009 \pm 1 \times 10^{-5}$	$0.00005 \pm 1 \times 10^{-5}$	$0.00004 \pm 1 \times 10^{-5}$	$0.00005 \pm 2 \times 10^{-5}$	
popup	$0.00005 \pm 3 \times 10^{-5}$	$0.00024 \pm 5 \times 10^{-5}$	$0.0002 \pm 2 \times 10^{-4}$	$0.0005 \pm 1 \times 10^{-4}$	$0.0003 \pm 2 \times 10^{-4}$
honeycomb	$0.00013 \pm 6 \times 10^{-5}$	$0.0006 \pm 3 \times 10^{-4}$	$0.0004 \pm 6 \times 10^{-4}$	$0.0007 \pm 6 \times 10^{-4}$	$0.0009 \pm 3 \times 10^{-4}$

**Table 1.9:** Max friciton coeff

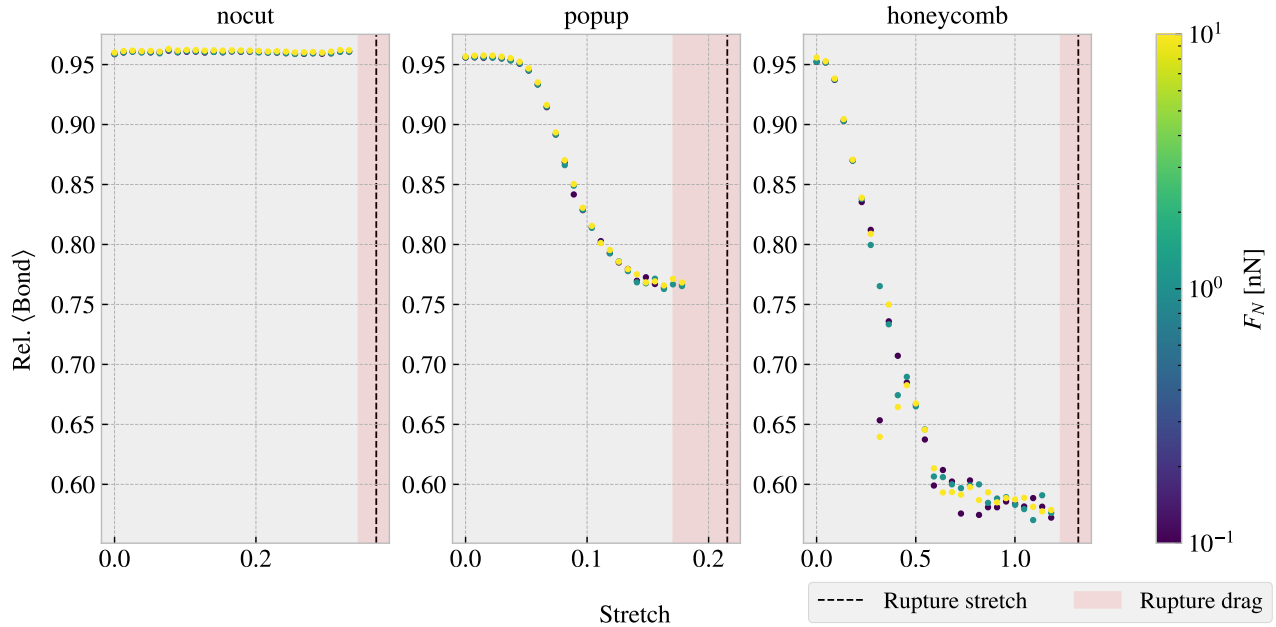
nocut	$0.0139 \pm 9 \times 10^{-4}$	$0.0083 \pm 7 \times 10^{-4}$	$0.010 \pm 1 \times 10^{-3}$	$0.0105 \pm 9 \times 10^{-4}$	
popup	$0.007 \pm 2 \times 10^{-3}$	$0.010 \pm 2 \times 10^{-3}$	$0.007 \pm 2 \times 10^{-3}$	$0.009 \pm 3 \times 10^{-3}$	$0.006 \pm 2 \times 10^{-3}$
honeycomb	$0.010 \pm 1 \times 10^{-3}$	$0.007 \pm 2 \times 10^{-3}$	$0.007 \pm 3 \times 10^{-3}$	$0.000 \pm 3 \times 10^{-3}$	$0.004 \pm 3 \times 10^{-3}$

The friction probably does not increase with normal force at an expected rate due to the fact the normal force is only applied on the pull blocks. Especially with the cutted sheet the tension drops such that the effecive normal force on the inner sheet is not changing so much. By this theory the friction force vs. normal force on the pull graph look a bit more like expected.

When looking at the graphs for the PB the max friction is visually textbook linear, while the mean friction is a bit more linear but also with negativ coefficients.

### 1.7.5.3 Contact area

Show plots of contact area vs stretch and discuss the fact that friction actually increases while contact area drops. Is the conclusion that there might be another more dominant cause of the increasing friction.

**Figure 1.29**

### 1.7.6 Computational cost

Talk about the computatational cost of different choices. How does comutation time scale with drag speed,  $dt$  and maybe  $T$  and  $K$  as well. One could also mention scaling with system size.

Show how the number of cores per simulation scale to argue that running on just one core (maybe 4) is smart for the next step of many simulations.

Mention the trouble with GPU to show that this was considered.

## 1.8 Generating data

Present the configuration and variable choices for the generated dataset. Perhaps include appendix with all the configurations shown in a grid or something similar.

## 1.9 Training forward network

## 1.10 Inverse design

## 1.11 Negative friction coefficient

### 1.11.1 Simulated coupling of normal force and stretch

### 1.11.2 Nanomachine coupling

Attempt to couple normal force and stretch by crossed carbon nanotube (CNT) contraption 1.30.

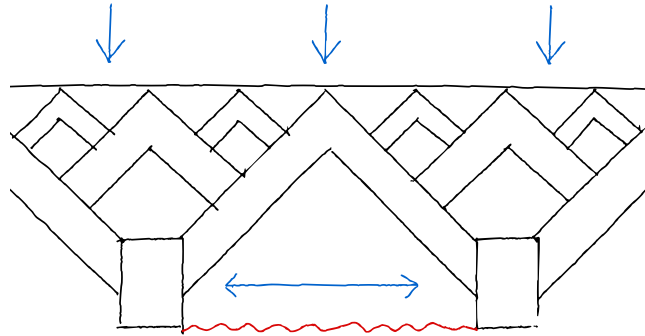


**Figure 1.30:** Working sketch for nanomachine



# **Summary**

## **1.12 Summary and conclusion**

## **1.13 Outlook / Perspective**

- What did we not cover?
- What kind of further investigations does this study invite?



# Bibliography

- [1] E. Gnecco and E. Meyer, *Elements of Friction Theory and Nanotribology*. Cambridge University Press, 2015, 10.1017/CBO9780511795039.
- [2] Bhushan, *Introduction*, ch. 1, pp. 1–? John Wiley & Sons, Ltd, 2013.  
<https://onlinelibrary.wiley.com/doi/pdf/10.1002/9781118403259.ch1>.  
<https://doi.org/10.1002/9781118403259.ch1>.
- [3] H.-J. Kim and D.-E. Kim, *Nano-scale friction: A review*, .
- [4] K. Holmberg and A. Erdemir, *Influence of tribology on global energy consumption, costs and emissions*, .
- [5] P. Z. Hanakata, E. D. Cubuk, D. K. Campbell and H. S. Park, *Forward and inverse design of kirigami via supervised autoencoder*, *Phys. Rev. Res.* **2** (Oct, 2020) 042006.
- [6] N. Manini, O. M. Braun, E. Tosatti, R. Guerra and A. Vanossi, *Friction and nonlinear dynamics*, *Journal of Physics: Condensed Matter* **28** (jun, 2016) 293001.
- [7] B. Bhushan and A. V. Kulkarni, *Effect of normal load on microscale friction measurements*, *Thin Solid Films* **278** (1996) 49–56.
- [8] J. H. Dieterich, *Time-dependent friction in rocks*, *Journal of Geophysical Research (1896-1977)* **77** (1972) 3690–3697, [<https://agupubs.onlinelibrary.wiley.com/doi/pdf/10.1029/JB077i020p03690>].
- [9] Y. Mo, K. T. Turner and I. Szlufarska, *Friction laws at the nanoscale*, .
- [10] W. Commons, *File:asperities.svg — wikimedia commons, the free media repository*, 2022.
- [11] G. Carbone and F. Bottiglione, *Asperity contact theories: Do they predict linearity between contact area and load?*, *Journal of the Mechanics and Physics of Solids* **56** (2008) 2555–2572.
- [12] J. A. Greenwood and J. B. P. Williamson, *Contact of nominally flat surfaces*, Dec, 1966. 10.1098/rspa.1966.0242.
- [13] B. N. J. Persson, *Theory of rubber friction and contact mechanics*, *The Journal of Chemical Physics* **115** (2001) 3840–3861, [<https://doi.org/10.1063/1.1388626>].
- [14] B. Luan and M. O. Robbins, *The breakdown of continuum models for mechanical contacts*, .
- [15] J. Norell, A. Fasolino and A. Wijn, *Emergent friction in two-dimensional frenkel-kontorova models*, *Physical Review E* **94** (04, 2016) .
- [16] M. Dienwiebel, N. Pradeep, G. S. Verhoeven, H. W. Zandbergen and J. W. Frenken, *Model experiments of superlubricity of graphite*, *Surface Science* **576** (2005) 197–211.
- [17] J. A. van den Ende, A. S. de Wijn and A. Fasolino, *The effect of temperature and velocity on superlubricity*, *Journal of Physics: Condensed Matter* **24** (oct, 2012) 445009.
- [18] B. Bhushan, *Nanotribology and nanomechanics*, *Wear* **259** (2005) 1–?
- [19] P. Zhu and R. Li, *Study of nanoscale friction behaviors of graphene on gold substrates using molecular dynamics*, .
- [20] J. Zhang, E. Osloub, F. Siddiqui, W. Zhang, T. Ragab and C. Basaran, *Anisotropy of graphene nanoflake diamond interface frictional properties*, *Materials* **12** (2019) .
- [21] F. Bonelli, N. Manini, E. Cadelano and L. Colombo, *Atomistic simulations of the sliding friction of graphene flakes*, .
- [22] X. Feng, S. Kwon, J. Y. Park and M. Salmeron, *Superlubric sliding of graphene nanoflakes on graphene*, .
- [23] M. Reguzzoni and M. C. Righi, *Size dependence of static friction between solid clusters and substrates*, *Phys. Rev. B* **85** (May, 2012) 201412.

- [24] S. Li, Q. Li, R. W. Carpick, P. Gumbsch, X. Z. Liu, X. Ding et al., *The evolving quality of frictional contact with graphene*, .
- [25] J. Tersoff, *New empirical approach for the structure and energy of covalent systems*, *Phys. Rev. B* **37** (Apr, 1988) **6991–7000**.
- [26] S. Corporation, “pair\_style lj/cut command.”
- [27] X. Wang, S. Ramírez-Hinestrosa, J. Dobnikar and D. Frenkel, *The lennard-jones potential: when (not) to use it*, *Phys. Chem. Chem. Phys.* **22** (2020) **10624–10633**.
- [28] R. Naeem, “Lennard-jones potential.”
- [29] Q. Zhang, D. Diao and M. Kubo, *Nanoscratching of multi-layer graphene by molecular dynamics simulations*, *Tribology International* **88** (2015) **85–88**.
- [30] S. Corporation, “pair\_style sw command.”
- [31] F. H. Stillinger and T. A. Weber, *Computer simulation of local order in condensed phases of silicon*, *Phys. Rev. B* **31** (Apr, 1985) **5262–5271**.
- [32] S. Corporation, “pair\_style tersoff command.”
- [33] T. Schneider and E. Stoll, *Molecular-dynamics study of a three-dimensional one-component model for distortive phase transitions*, *Phys. Rev. B* **17** (Feb, 1978) **1302–1322**.